



POLITECNICO
MILANO 1863

SCUOLA DI INGEGNERIA INDUSTRIALE
E DELL'INFORMAZIONE

Study of the radiation field of the ALFA station at ELI Beamlines

TESI DI LAUREA MAGISTRALE IN
NUCLEAR ENGINEERING – INGEGNERIA NUCLEARE

Author: **Francesco BRAVIN**

Student ID: 995091
Advisor: Prof. Marco CARESANA
Co-advisor: Dr. Roberto VERSACI
Academic Year: 2023-24

This thesis was conducted at the Extremelight Infrastructure Beamlines in Prague, Czech Republic, specifically within the radiation protection working group.



Abstract

Precise dosimetry is critical to ensure safety and optimize operational efficacy in laser-driven accelerator settings. This thesis investigates the secondary radiation field produced by a laser-driven electron accelerator, specifically focusing on the ALFA experimental station at the ELI Beamlines facility in the Czech Republic.

The research employs a combination of dosimetric measurements and Monte Carlo simulations to analyze the secondary radiation produced during the acceleration process. The three adopted dosimeters were tested under conditions characterized by high charge per bunch, short temporal duration, and a repetition frequency of 1 kHz, which pose significant challenges for conventional radiation detection devices.

The analysis of the collected data revealed notable discrepancies in neutron radiation measurements between the Lupin and Pandora dosimeters, with differences reaching four orders of magnitude. Further investigation indicated that these discrepancies were linked to the high-energy neutron channel of the Pandora dosimeter, while the Lupin dosimeter's results remained within an acceptable range when compared to the low-energy neutron channel of the Pandora. In terms of gamma radiation, the Nausicaa dosimeter recorded doses 1.5 times higher than those of the Pandora, which was consistent with expectations given the operational context.

The findings suggest that the anomalous behavior of the Pandora dosimeter is not due to device malfunction but is likely associated with high dose rate levels. The study highlights the importance of further research to understand these phenomena, including controlled experiments and a detailed examination of the dosimeter's electronics.

Sommario

Una dosimetria precisa è fondamentale per garantire la sicurezza e ottimizzare l'efficacia operativa negli ambienti degli acceleratori laser-driven. Questa tesi indaga il campo di radiazione secondaria prodotto da un acceleratore di elettroni laser-driven, concentrandosi in particolare sulla stazione sperimentale ALFA presso la struttura ELI Beamlines in Repubblica Ceca.

La ricerca impiega una combinazione di misurazioni dosimetriche e simulazioni Monte Carlo per analizzare la radiazione secondaria prodotta durante il processo di accelerazione. I tre dosimetri adottati sono stati testati in condizioni caratterizzate da un'alta carica per impulso, una breve durata temporale e una frequenza di ripetizione di 1 kHz, che pongono sfide significative per i dispositivi di rilevamento della radiazione convenzionali.

L'analisi dei dati raccolti ha rivelato notevoli discrepanze nelle misurazioni della radiazione neutronica tra i dosimetri Lupin e Pandora, con differenze che raggiungono quattro ordini di grandezza. Ulteriori indagini hanno indicato che queste discrepanze erano collegate al canale di neutroni ad alta energia del dosimetro Pandora, mentre i risultati del dosimetro Lupin rimanevano all'interno di un intervallo accettabile se confrontati con il canale di neutroni a bassa energia del Pandora. In termini di radiazione gamma, il dosimetro Nausicaa ha registrato dosi 1,5 volte superiori a quelle del Pandora, il che era coerente con le aspettative date le condizioni operative.

I risultati suggeriscono che il comportamento anomalo del dosimetro Pandora non è dovuto a un malfunzionamento del dispositivo, ma è probabilmente associato a livelli elevati di dose. Lo studio evidenzia l'importanza di ulteriori ricerche per comprendere questi fenomeni, inclusi esperimenti controllati e un esame dettagliato dell'elettronica del dosimetro.

Contents

1. Introduction	1
2. Laser-Driven Acceleration and the ELI Project	4
2.1. Lasers	4
2.1.1 Lasers development.....	5
2.2. Laser-driven Accelerators	7
2.2.1. LWFA overview	8
2.2.2. LWFA current and future challenges.....	9
2.3. ELI ERIC.....	10
2.3.1 What is an ERIC	11
2.3.2. The ELI project.....	11
2.4. ELI Beamlines.....	12
2.4.1 Primary Sources	13
2.4.2. Secondary Sources.....	15
2.5. ALFA.....	16
3. Dosimetry at Laser-Driven Accelerator Facilities	18
3.1. Dosimetry	18
3.1.1. Basic dosimetric quantities.....	19
3.1.2. Protection quantities.....	20

3.1.3. Operational quantities	22
3.2. Dosimetry at Laser Facilities	26
3.2.1. Timing of the dose delivery	27
3.2.2. Source term.....	30
3.2.3. Electromagnetic Pulses	32
4. Monte Carlo as a Tool for Dosimetry	34
4.1. Monte Carlo Overview	34
4.1.1. The Method.....	34
4.1.2. Pseudo-Random Numbers.....	35
4.1.3. Inverse Transform Method	36
4.1.4. Convergence of the Method.....	38
4.2. MCS in Dosimetry.....	39
4.2.1. FLUKA.....	39
4.3. MCS with FLUKA at Laser Facilities.....	41
5. Dosimetry Study at ALFA.....	42
5.1. Purpose and Outline of the Study	42
5.2. Dosimeters Setup	44
5.2.1. LUPIN.....	45
5.2.2. Nausicaa	47
5.2.3. Pandora.....	47
5.3. ALFA Setup.....	50
5.4. Monte Carlo Simulation Setup.....	53

5.4.1. Geometry	53
5.4.2. Source and Run	54
6. Measurements and Data Analysis.....	56
6.1. Dataset.....	56
6.2. Neutrons.....	57
6.3. Gamma Particles.....	64
6.4. High Energy Neutrons.....	67
7. Conclusions	76
References	80
List of Figures.....	84
List of Tables.....	87

1. Introduction

The rapid proliferation of high-power laser technology worldwide [1] has led to a growing interest in laser-driven accelerators due to their potential applications across various fields. Advances in laser technology have enabled a higher degree of control over laser parameters, extended laser propagation distances, and a deeper understanding of the underlying physics, resulting in the production of higher quality and more energetic particle bunches [2]. Potential applications for this technology span over a wide range, including medicine, biology, condensed matter physics, and high energy density science [3]. Due to the small scale of the acceleration process (in the sub-millimeter range), laser-driven acceleration is well-suited for innovative research and hold significant potential for advancing future generations of particle accelerators across various applications. For example, radiation therapy using charged particles could greatly benefit from compact laser-driven accelerators, as they would eliminate the need for large cyclotrons in dedicated hospital facilities, thus offering practical and economic advantages. Once fully developed, laser-driven acceleration technology is expected to reduce accelerator sizes and costs, facilitating the broader adoption of charged particle tumor treatments, which are currently limited by the high expenses associated with cyclotron and synchrotron installations [4].

These perspectives have highlighted the critical need for precise dosimetry in laser-driven accelerator environments. Dosimetry, defined as the measurement and assessment of the dose delivered by ionizing radiation

within a medium, is essential for ensuring the safety of both operators and patients –for instance, in medical applications–, as well as for optimizing the efficacy of laser-driven accelerator technologies. However, these technologies present a significant challenge for any commercial dosimeter due to the exceptional conditions to which the devices would be subjected. The technological challenges include the ultra-short duration of the laser pulses, the mixed radiation field generated by the interaction of the primary beam with its surroundings, and the intense electromagnetic pulses resulting from the laser-plasma interaction.

While dosimeters designed for operation in pulsed fields are commercially available, none are specifically tailored to function effectively under these conditions. Laser-driven particles are produced in bunches characterized by a high charge per bunch, short temporal duration, and a repetition frequency of up to 1 kHz, which can potentially saturate the response of active radiation detection devices [5]. Furthermore, the literature on dosimetry in the vicinity of laser-driven particle accelerators is limited due to the novelty of the technology. Most studies on secondary radiation fields have been conducted in conventional acceleration facilities to assess the secondary radiation dose to which operators or patients are exposed. However, only a few studies investigate the response of commercially available dosimeters in pulsed field environments, and even fewer focus on dosimetry in laser-driven acceleration experiments [5].

This work fits precisely within this context, aiming to investigate the secondary radiation field generated by a laser-driven electron accelerator, as well as to examine the performance of three commercially available dosimeters in this environment. This investigation is conducted through the analysis of dosimetric measurements collected by the three different dosimeters,

supplemented by Monte Carlo simulations to support the underlying physical and technical considerations.

The study has been carried out at the ELI Beamlines facility in the Czech Republic, which operates state-of-the-art, high-peak-power femtosecond laser systems with high-energy and high-repetition-rate capabilities, as well as secondary sources (X-rays and accelerated particles) with unique features. More specifically, the dosimeters measured the secondary radiation field of the ALFA experimental station, a laser wakefield electron accelerator that operates at a repetition rate of 1 kHz and accelerates electron bunches within an energy range of 1 to 100 MeV.

Chapter 2 provides an overview of lasers and laser-driven acceleration technologies, with a particular focus on laser wakefield electron accelerators, as well as a description of the ELI project and the ELI Beamlines facility. Chapter 3 discusses dosimetry, beginning with introductory concepts and then addressing the specific challenges of dosimetry in a laser-driven acceleration environment. Chapter 4 presents an overview of the Monte Carlo method and the challenges associated with applying this simulation technique in the context of laser-driven accelerators. Chapter 5 presents a thorough description of the dosimeters and the experimental setup utilized during the data collection campaign. Finally, Chapter 6 concludes with the presentation of the data measurements and a discussion of the results, while Chapter 7 provides a summary of the findings of this research.

2. Laser-Driven Acceleration and the ELI Project

2.1. Lasers

A laser, which stands for “Light Amplification by Stimulated Emission of Radiation”, is a device that generates light through the stimulated emission process [6]. It operates exploiting the amplification of light that takes place in the ‘oscillator’, a resonant cavity composed of two mirrors perpendicular to the electromagnetic wave propagation direction, where the gain medium is inserted. The gain medium amplifies light by providing a medium in which stimulated emission of photons can occur, typically consisting of atoms or molecules that can be excited to higher energy levels. A schematic view of a laser is shown in **Figure 2.1**.

When an external energy source (known as a pump) excites the atoms or molecules in the gain medium, a significant number of them are elevated to a higher energy level. If the excited state has a relatively short lifetime, the atoms will quickly decay to a lower energy state. ‘Population inversion’ is ultimately achieved if the population of the excited state remains higher than that of the lower state. This condition is crucial for stimulated emission because it can stimulate the emission of another photon, resulting in two coherent photons that are in phase and have the same energy.

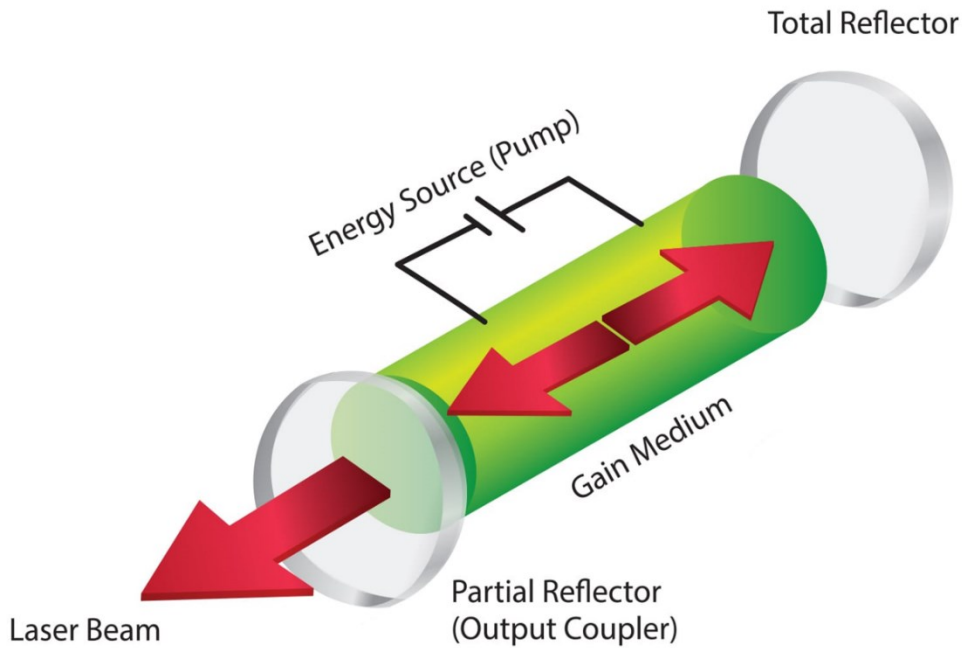


Figure 2.1: Schematic representation of a laser and its main components (adapted from <https://www.ulsinc.com/learn>).

2.1.1 Lasers development

Since the early experiments in the 1960s, high-intensity laser facilities have evolved significantly. Initially, Q-switching [7] was introduced to create pulsed laser output by temporarily storing energy in the gain medium and then releasing it in a short, intense burst via stimulated emission. This is achieved by modulating the quality factor (Q) of the laser cavity, which controls the loss of light. When the Q factor is low, energy builds up in the gain medium through continuous pumping. Once a certain threshold is reached, the Q factor is suddenly increased, allowing the stored energy to be released as a powerful pulse.

Subsequently, mode-locking [8] was developed, allowing for the production of extremely short pulses of light (down to the orders of femtoseconds). It works

by synchronizing the different longitudinal modes of the laser cavity so that they oscillate in phase, resulting in constructive interference and the formation of intense, coherent pulse trains. As the modes interfere constructively, the energy is compressed into shorter time intervals, resulting in the formation of ultra-short pulses.

Another notable advancement was introduced by the Optical Parametric Amplification (OPA) [9] technique, which has been essential to reach high laser intensities. In OPA, a high-energy pump laser beam interacts with a nonlinear medium, such as a crystal, to generate two new beams: a signal beam and an idler beam. This nonlinear optical process allows to amplify the signal beam through stimulated emission and to remove the excess energy with the aid of the idler beam.

Finally, Chirped Pulse Amplification (CPA) [10] was integrated (OPCPA). The process involves three main steps: first, the pulse is stretched in time to reduce its peak intensity, which helps prevent damage to the gain medium during amplification. Next, the stretched pulse is amplified using a gain medium, increasing its energy. Finally, the amplified pulse is recompressed back to its original duration, resulting in a high-intensity pulse.

Figure 2.2 shows the progression of the focused intensity over the years, marking the major technological advancements. The focused intensity (W/cm^2) is the concentration of laser power per unit area at the focal point of the laser beam.

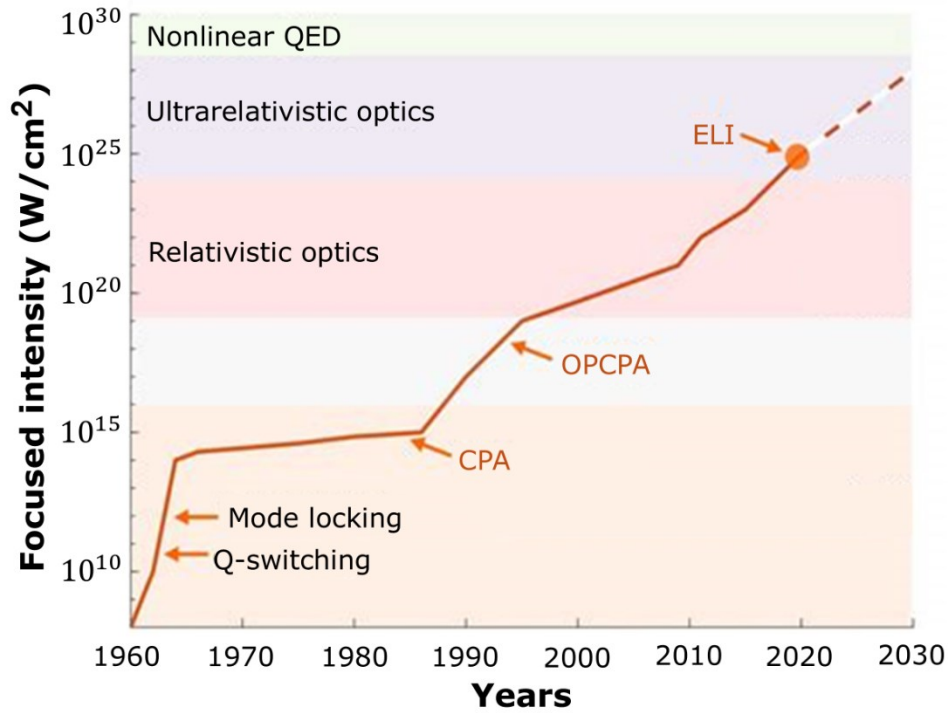


Figure 2.2: Focused intensity progress in time (from eli-alps.hu).

2.2. Laser-driven Accelerators

The development of ultrashort high-energy lasers has been a key step in the realization of laser-driven particle accelerators. Among all laser-driven accelerators, Laser-Plasma Accelerators (LPA) stand out as one of the most promising options as an alternative to conventional accelerators [11]. Unlike traditional accelerators, which rely on electromagnetic fields generated by conducting electrodes or within cavities to accelerate charged particles, LPAs utilize the interaction between laser and plasma to achieve acceleration.

The main limitation of conventional acceleration technologies is the low accelerating gradient per meter, which increases both the length and material costs required for more powerful accelerators. In fact, the maximum field is

limited to under 100 MV/m by electrical breakdown of the dielectric medium [11]. In comparison, LPAs can produce accelerating fields that are 1000 times greater than other technologies (i.e., can reach orders of GV/m), allowing for a corresponding reduction in the size of the accelerator.

Plasma acceleration technology dates back to the 1950s, originating from the theoretical contributions of Budker and Veksler [12], who proposed utilizing plasma collective fields for a more compact acceleration of charged particles. Subsequently, in the 1970s and 1980s, Tajima and Dawson introduced schemes for a Laser Wakefield Accelerator (LWFA), a specific configuration of LPA [13]. However, their proposal has only been fully realized experimentally with the advent of ultrashort high-current electron bunches and high-power ultrashort pulsed lasers [14].

2.2.1. LWFA overview

In a LWFA accelerator, an ultrahigh intensity laser pulse is focused in an underdense plasma. The ponderomotive force, which is the force that charged particles experience due to the electromagnetic field of the laser, causes a charge separation in the plasma by displacing electrons [15]. As the electrons are pushed away from the laser axis, they leave behind much heavier ions, resulting in the induction of an extremely high electrostatic field due to the charge separation. This field acts as a restoring force for the displaced electrons. As the electrons are expelled and repeatedly return to the laser axis, they generate periodic modulations in electron density that follow the laser pulse, referred to as a plasma wave or a wakefield [16]. If an electron bunch self-injects into this wave (or bubble), it can be rapidly accelerated in the direction of laser propagation by the huge electric field within the bubble, which can exceed 100 GV/m. A schematic representation of this process is

shown in **Figure 2.3**. Electric fields of this intensity are highly effective for accelerating electrons to relativistic energies over short distances (usually less than a millimeter). The resulting accelerated electron beams have femtosecond (fs) durations and are inherently synchronized with the laser pulse.

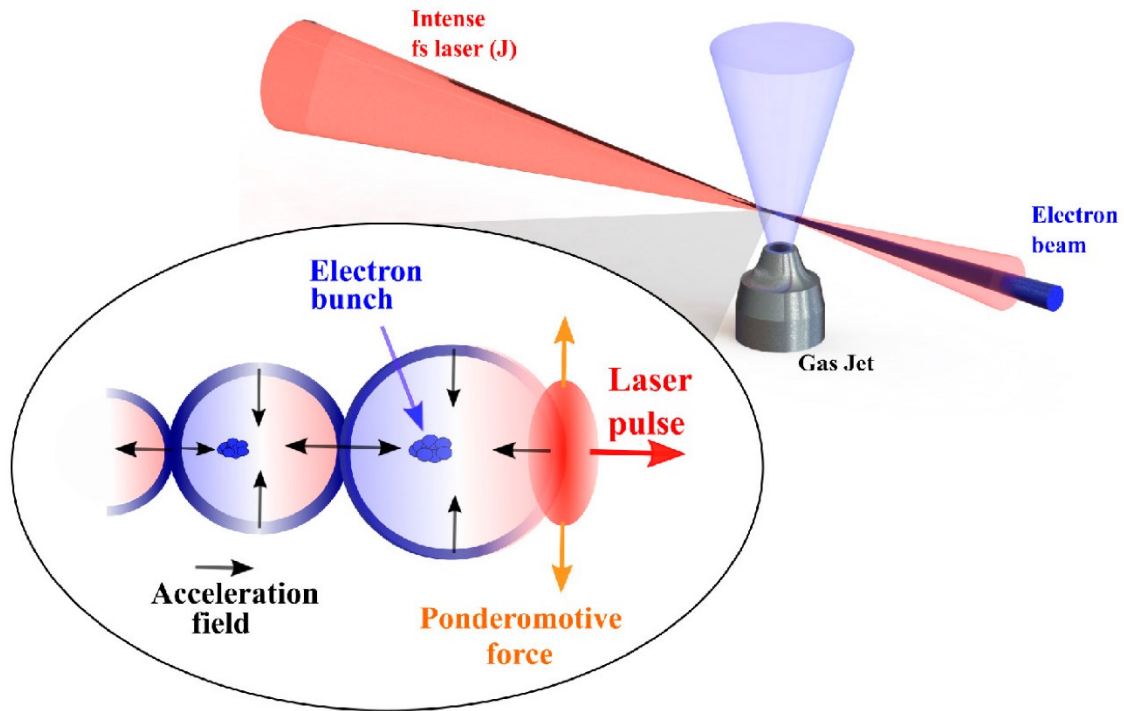


Figure 2.3: Schematic representation of the acceleration of electrons in a LWFA. In this case, the plasma is produced by ionization of the gas released by a gas inlet in correspondence of the focusing point of the laser (from [16]).

2.2.2. LWFA current and future challenges

In the past decade, LWFA has advanced significantly, moving beyond initial proof-of-principle experiments to achieve electron beams with energies of several hundred MeV [14], good normalized transverse emittance ($\epsilon_n \approx 1 \mu\text{m}$), and relatively narrow energy spreads ($\Delta E/E \approx 1\%$). These improvements have led to enhanced beam reproducibility and availability, resulting in preliminary

applications experiments. However, these have primarily remained at the proof-of-principle stage. A key challenge is to advance these experiments to a point where LWFA can provide beam time for broader user access, potentially impacting fields such as material science, medicine, radiation biology, and chemistry.

For LWFA to be meaningful, its electron beam parameters must surpass those of conventional accelerators. For example, modern RF electron guns produce electron bunches a few tens of femtoseconds long, with low emittance ($\epsilon_n < 20$ nm), high repetition rates (> 100 Hz), and excellent stability, enabling high-resolution ultrafast electron diffraction [14]. Thus, LWFA needs to achieve not only higher temporal resolution but also comparable emittance, stability, and repetition rates. Focusing on lower energies, such as 5 MeV, would prioritize femtosecond duration and stability over high-gradient acceleration. While some groups are working toward these goals, the necessary performance levels have yet to be realized.

2.3. ELI ERIC

Over the past few decades, there has been a surge of interest in the field of laser-driven accelerators, leading to substantial investments in research globally [14]. As detailed in the previous paragraph, the development of ultrahigh power lasers is crucial to the success of this technology, as well as in many other applications. In this context, the Extreme Light Infrastructure (ELI) European Research Infrastructure Consortium (ERIC) exemplifies a remarkable initiative to elevate European research in the field of lasers to an exceptional level.

2.3.1 What is an ERIC

A European Research Infrastructure Consortium is a legal entity established under European Union law to facilitate collaboration in research and innovation across Europe [17]. ERICs provide a framework for the establishment and operation of large-scale research infrastructures that are of European interest and benefit. They enable collaboration among various stakeholders, including research institutions, universities, and industry partners, allowing for the sharing of resources, knowledge, and expertise.

Examples of ERICs include ELIXIR, a research infrastructure focused on life science data management and analysis. It was officially established as an ERIC in 2013. The European Spallation Source (ESS) is also an ERIC since 2015, providing neutrons for scientific research across various disciplines. EuroBioImaging serves as a pan-European research infrastructure for biological and biomedical imaging and was recognized as an ERIC in 2019.

2.3.2. The ELI project

The Extreme Light Infrastructure project represents the largest international network of civilian laser-based user facilities. The design and construction of the ELI facilities started in the early 2000s; however, the project was formally established as an ERIC in 2021 [18]. ELI provides researchers and industries with the opportunity to utilize the most extensive collection of high-power and ultrafast lasers worldwide. The founding members of this international organization are the Czech Republic, Hungary, Italy, and Lithuania, which contribute both scientifically and financially to the consortium, while Germany and Bulgaria are founding observers aiming to join fully in the future.

The ELI ERIC facilities are situated in Hungary and the Czech Republic. The Attosecond facility (Hungary) aims at providing a broad range of ultrafast light sources, to enable temporal investigations of electron dynamics in atoms, molecules, plasmas and solids up to attosecond time scales; the Beamlines facility (Czech Republic) is dedicated to the production of short X-rays and acceleration of particles (protons, electrons and ions) employing high-power lasers at a repetition rate of up to 1 kHz [18].

2.4. ELI Beamlines

ELI Beamlines is, in the same way as the other ELI ERIC facilities, a laser-based user facility, meaning that it provides access to specialized equipment, tools, and resources for external researchers, referred to as “users”. In fact, ELI Beamlines features multiple primary and secondary sources, along with various support laboratories, workshops, and essential equipment for efficient operations [19]. The primary objective of these activities is to improve user access to the available experimental stations and to finalize the commissioning of additional equipment and experimental setups.

ELI Beamlines is equipped with four primary laser systems that support a dozen experimental stations, with the potential to accommodate additional stations in the future. The laser systems and experimental stations are situated in a dedicated building that also houses essential auxiliary systems, including cooling, ventilation, and vacuum systems.

An expanded view of the laser building of ELI Beamlines is shown in **Figure 2.4**. As the name states, the laser building houses the laser systems, as well the experimental halls and the support rooms. It is an integral component of the ELI Beamlines site, which comprises both the laser building and an office

building. The two structures are designed with distinct architectural characteristics that align with their respective functions, while also being interconnected to facilitate the movement of personnel and materials. The entire site is situated in Dolní Břežany, near Prague, Czech Republic.

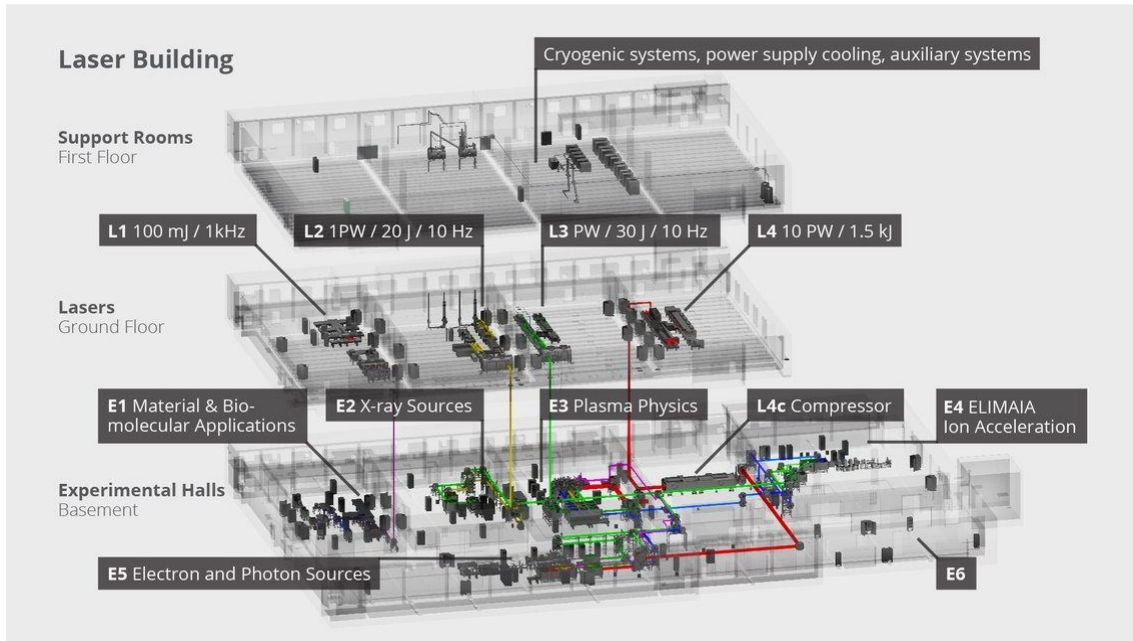


Figure 2.4: ELI Beamlines laser building schematic view (from eli-beams.eu).

2.4.1 Primary Sources

The L1-Allegro laser has been developed in-house by the ELI Beamlines laser team. Its design is based entirely on the amplification of frequency-chirped picosecond pulses within an optical parametric chirped pulse amplification (OPCPA, see Paragraph 2.2.1) chain that includes a total of seven amplifiers. The OPCPA amplifier stages are pumped by precisely synchronized picosecond pulses produced by advanced thin-disk-based Yb:YAG laser systems.

The L2-DUHA Laser (Dual-beam Ultra-fast High energy OPCPA Amplifier) is designed to deliver 100 TW-level pulses at a high repetition rate of 50 Hz, operating at a wavelength of 820 nm. As the newest addition to the ELI Beamlines laser systems, L2-DUHA is currently under development.

The L3-HAPLS laser (High-Repetition-Rate Advanced Petawatt Laser System) was developed at the Lawrence Livermore National Laboratory [20], with ELI Beamlines collaborating on the development of the petawatt pulse compressor, short-pulse diagnostics, and controls and timing for the short-pulse components. The L3-HAPLS pump engine is designed to deliver a pulse energy of 200 J and operates at a frequency of 10 Hz, utilizing two Nd-doped glass amplifiers cooled by helium gas. Each amplifier is powered by high-power laser diode arrays, each providing an impressive peak power of 800 kW, making them the highest peak-power pulsed laser diode arrays in the world.

The L4-Aton laser system is designed to achieve an extraordinary peak power of 10 PW, generating pulses with a duration of 150 fs, pulse energy of 1.5 kJ, and a repetition rate of one shot per minute. The system architecture is based on CPA through several successive stages of optical parametric amplifiers, followed by direct amplification using two types of Nd:glass laser discs. The laser was developed by a consortium that includes National Energetics (USA) [21] and EKSPLA (Lithuania) [22], with significant contributions from ELI Beamlines and is currently in trial operation. A summary of the specifications of the four laser systems is presented in **Table 2.1**, with focus on up-to-date performances and the target ones.

Laser system	Peak Energy (J)	Peak Power (TW)	Maximum Repetition Rate (Hz)
L1-Allegra			
Present	0.03	1.5	10^3
Target	0.1	5	10^3
L2-DUHA			
- Target	2	100	50
L3-HAPLS			
- Present	30	333	3.3
- Target	30	10^3	10
L4-Aton			
- Target	$1.5 \cdot 10^3$	10^4	1 shot per minute

Table 2.1: Present and Target Parameters of the Laser Systems at ELI Beamlines (from [23]).

2.4.2. Secondary Sources

Secondary sources refer to beams generated from primary lasers, producing various types of radiation or particles for experimental purposes. Among all the secondary sources present at ELI Beamlines, only the Allegra Laser For Acceleration (ALFA) is of primary interest for this work and its characteristics will be explained thoroughly in the following paragraphs. **Table 2.2** summarizes the primary features of all secondary sources.

Station	Laser	Main Goal
HHG	L1-Allegra	Ultrashort pulses of tunable coherent extreme ultraviolet soft X-ray radiation.
PXS	L1-Allegra	High-brightness X-ray beams with energies varying from 3 to about 77 keV.
E2 X-ray source	L3-HAPLS	Ultrafast and bright hard X-ray.
LUIS	L2-DUHA	Laser-driven electron beams for the generation of initially spontaneous, and subsequently, coherent photon radiation.
	L3-HAPLS L4-Aton	
ELBA	L2-DUHA	Acceleration of electrons up to energies of tens of gigaelectron-volts.
	L3-HAPLS L4-Aton	
ALFA	L1-Allegra	Electron beams up to energies of 100 MeV
ELIMAIA	L3-HAPLS	Protons acceleration up to 60 MeV (phase 1) and up to 250 MeV (phase 2).
	L4-Aton	
P3	L3-HAPLS	High-field laser plasma interaction high-energy density physics.
	L4-Aton	

Table 2.2: Main experimental stations of ELI Beamlines (from [23,24]).

2.5. ALFA

The ALFA electron beam source employs laser wakefield acceleration technology to generate relativistic pulsed electron beams. In this system the beam is produced by focusing of the laser beam (up to 32 mJ pulse energy and 15 - 20 fs pulse length range at 1 kHz) generated by L1-Allegra laser system into a gas target. The target kinetic energy of the electron beam is designed to be within the range of 1 to 100 MeV [24], which represents an unprecedented energy level for LWFA operating at a frequency of 1 kHz [25]. The experimental station associated with the ALFA source enables users to

perform laser-matter interaction experiments at relativistic intensities () and at a high repetition rate.

In a recent study conducted by Lazzarini and others [25], ultra-short electron beams at 1 kHz repetition frequency and energies up to 50 MeV were demonstrated at ALFA. The setup included: a 76.2 mm off-axis parabola (OAP) used to focus the laser right above the nozzle exhaust of the gas jet. In this configuration, the most energetic and collimated electron beams were obtained by firing the laser on a gas mixture of helium (98%) and nitrogen (2%). The setup also included calibrated electron spectrometer consisting of a 5 mm aluminum slit, a permanent magnetic dipole and a LANEX screen coupled with a 12-bit CMOS global shutter camera. The output has resulted in the production of quasi-monoenergetic (25% energy spread), collimated (2 mrad divergence) electron beams. A schematic representation of the setup is displayed in **Figure 2.5**.

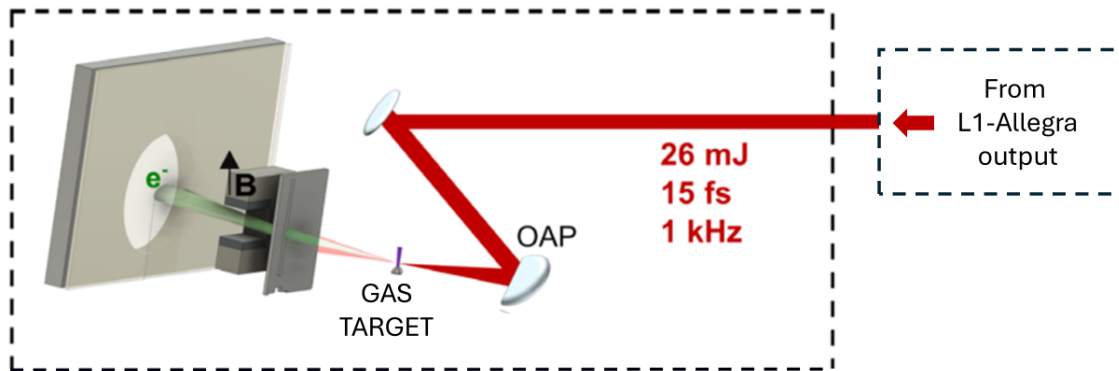


Figure 2.5: Scheme of ALFA experimental station (adapted from [25]).

3. Dosimetry at Laser-Driven Accelerator Facilities

3.1. Dosimetry

The goal of dosimetry of ionizing radiation is to determine the energy released by the radiation in the medium with which it interacts [26]. It is therefore necessary to introduce specific quantities - known as dosimetric quantities - whose measurement or calculation allow for the determination of the energy absorbed by the irradiated medium.

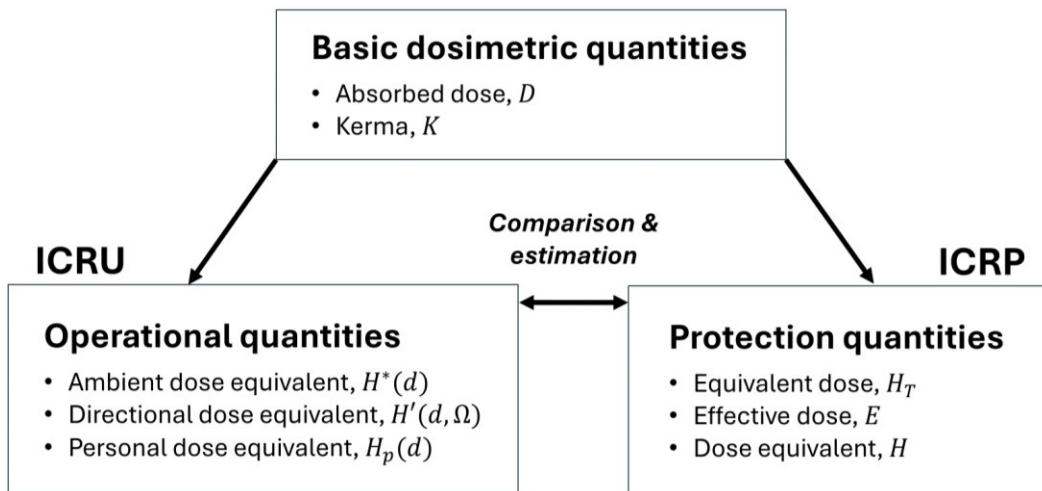


Figure 3.1: Relationship between the protection quantities and operational quantities for use in dosimetry (adapted from [27]).

These quantities are grouped in two distinct categories, which are the protection quantities and the operational quantities [27]. Both groups of definitions rely on the so called *basic dosimetric quantities*, detailed in the followings. **Figure 3.1** illustrates a diagram of the most commonly used dosimetry quantities and their interrelationships.

3.1.1. Basic dosimetric quantities

The amount of energy that ionizing radiation can lose in a single event in the medium it passes through varies randomly. In a given event, a particle can indeed lose a more or less significant portion of its energy, and in some cases, all of it. However, using a quantity such as the energy lost in a single event would not be practical for dosimetry purposes. Therefore, it is necessary to define non-stochastic quantities that are correlated to the average values of the stochastic quantities of interest. These quantities are commonly referred to as basic dosimetric quantities and they include the absorbed dose and the kerma, which are fundamental for defining protection and operational quantities.

The *absorbed dose*, D , as defined by the ICRU (International Commission on Radiation Units and Measurements) Report 51 [28], is the energy deposited by radiation per unit mass of the deposition site:

$$D = \frac{d\bar{\epsilon}}{dm}, \text{ [Gy]}$$

Where $d\bar{\epsilon}$ is the average energy deposition due to ionizing radiation per unit of mass dm . The unit of measure of the absorbed dose is Gray (Gy). The *energy deposition* is defined simply as:

$$\epsilon = T_{in} - T_{out} - Q, \text{ [J]}$$

Here T_{in} is the energy of the incident ionizing particle, T_{out} is the sum of energies of all the ionizing particles leaving the site of deposition and Q represents the variations in the rest energy of the atom and all particles involved in the interaction.

It is important to note that absorbed dose alone does not encompass radiation damage, as this would necessitate details regarding the type and energy of the incoming particles. This is the reason why more specific quantities are defined for radiation protection purposes.

The *kerma* (Kinetic Energy Released in Matter), K , defined by the ICRU Report 33 [29] as the ratio between dE_{tr} and dm , where dE_{tr} is the sum of the initial kinetic energies of all ionizing charged particles produced by "neutral ionizing" particles (such as photons and neutrons) in a material of mass dm . The unit of measure is Gray.

$$K = \frac{dE_{tr}}{dm}, \text{ [Gy]}$$

This implies that the kerma considers the kinetic energy of secondary particles generated within the volume of interest, which are then transported out of that volume. This distinction is what sets apart dose from the kerma, as dose solely quantifies the energy deposited within the volume.

3.1.2. Protection quantities

Protection from ionizing radiation (or radioprotection) is based on a set of actions aimed at minimizing, with the help of physical means and operational procedures, the radiological risk for individuals. At the heart of radiation protection activities is a regulatory framework that indicates, among other things, the limits that are recommended not to exceed for exposures of individuals to ionizing radiation. These limits are established to avoid non-

stochastic effects of ionizing radiation and to minimize or make negligible stochastic effects. Expanding on the defined basic dosimetric quantities, protection quantities are introduced by the International Commission on Radiological Protection (ICRP), with the dual property of being dependent on the quantities of the radiation field (fluence, energy, etc.) on the one hand, and on the other hand, of containing the essential information necessary to correlate their value with an estimate of the radiological risk for the people involved.

The ICRP Publication 60 [30] defines the *equivalent dose* as:

$$H_T = \sum_R D_{T,R} \cdot w_R , \text{ [Sv]}$$

Where D represents the dose absorbed by tissue T from radiation R , and w is a weighting factor that adjusts for the varying biological effects induced by different radiation types. The summation is necessary when multiple radiation types are involved. To emphasize a qualitative distinction between equivalent dose and absorbed dose, the conventionally used unit is the Sievert (Sv), instead of Gray, even though both are equivalent to 1 J/kg.

Moreover, the concept of *effective dose*, E , was introduced to address the variation in tissue radiosensitivity to radiation based on the specific organ being irradiated. This is achieved by multiplying the equivalent dose by a tissue-specific weighting factor, w_T .

$$E = \sum_T H_T \cdot w_T , \text{ [Sv]}$$

The effective dose delivered to the body, measured in Sievert, is determined by summing over all the target tissues.

It is understood that the biological impact of a given absorbed dose, D , can vary depending on the type of radiation delivering it (such as γ -photon, α -particle, neutron) or the specific tissue it affects. The rate of energy deposition along the path of a particle, known as Linear Energy Transfer (LET), significantly influences the extent of biological damage caused as the particle traverses

through a tissue. In general, a higher LET of a particle corresponds to a greater biological damage, even when the absorbed dose, D , remains the same. To address this variation, the concept of *dose equivalent*, H , was introduced:

$$H = Q(LET) \cdot D, \text{ [Sv]}$$

Here, Q is a quality factor that considers the biological damage caused by the particular particle and is solely dependent on the LET.

3.1.3. Operational quantities

Protection quantities cannot be easily measured due to the inherent challenge of measuring the dose to individual tissues during external irradiation. Their value can, in fact, only be determined through estimates or calculations based on both theoretical and experimental data, or as an approximation of the measurement of another family of dosimetric quantities, the operational quantities. These quantities conceptually constitute a bridge that connects the basic dosimetric quantities with the protection quantities and have been defined by the ICRU for two types of measurements: area monitoring and individual monitoring.

Area monitoring is the process of measuring environmental radiation fields to estimate the radioprotection quantities H_T or E for individuals who may be exposed to those fields. Measurements are taken in the absence of individuals in the environment in question and should provide information to calculate the dose equivalent a person would receive in that radiation field with the person present. This type of monitoring allows evaluating a person's past or future exposure to a specific radiation field and is carried out using instruments placed in free air that provide dose values similar to those in human tissue. The ICRU sphere, with a diameter of 30 cm, is the reference phantom for these

measurements, simulating the properties of human tissue. The percentage composition by weight is defined as follows:

$$\left\{ \begin{array}{ll} \textit{Hydrogen}: & 10.1 \% \\ \textit{Carbon}: & 11.1 \% \\ \textit{Nitrogen}: & 2.6 \% \\ \textit{Oxygen}: & 76.2 \% \end{array} \right.$$

To correlate the detector signal to an operational quantity for estimating the protective quantity related to the human body, it is essential that the detector is exposed to the same radiation field that has affected or will affect the human body or the phantom simulating it. To ensure that the ICRU sphere is subject to a radiation field identical to the detector, it is necessary to conceptually extend the radiation field irradiating the detector to a volume at least equal to that containing the entire sphere. An *expanded field* is therefore defined as a radiation field that, for each type of radiation it consists of, at every point within a given volume of interest, has the same particle fluence, the same angular distribution, and the same energy distribution as in the actual field at the point where the measurement is taken.

Moreover, the calibration coefficient of the instrument allows correlating the instrument signal to the value that the operational dosimetric quantity assumes at a given depth in the ICRU sphere. This causes the value of the operational quantity (except for measurements in the center of the ICRU sphere) to depend on the angle of radiation incidence. To overcome this issue, the "aligned and expanded field" is defined with the same characteristics as the expanded field but with unidirectional radiation components at each point.

Different operational quantities are defined for weakly and strongly penetrating radiation types due to regulatory considerations. The radiation is defined as strongly penetrating if the ratio between the effective dose, E , and the equivalent dose delivered to the skin, H_{skin} , is larger than 10:

$$\frac{E}{H_{skin}} > 10$$

For instance, radiation such as photons with energy lower than 15 KeV or electrons with energy lower than 2 MeV are categorized as weakly penetrating, whereas neutrons or higher energy photons are classified as highly penetrating.

The *ambient dose equivalent*, $H^*(d)$, is the operational dosimetric quantity used to estimate the effective dose in area monitoring in a highly penetrating radiation field. It is defined as the dose equivalent that would be produced by the corresponding aligned and expanded field in the ICRU sphere at depth d on the radius of the sphere located in the opposite direction to that of the aligned field, as displayed in **Figure 3.2**.

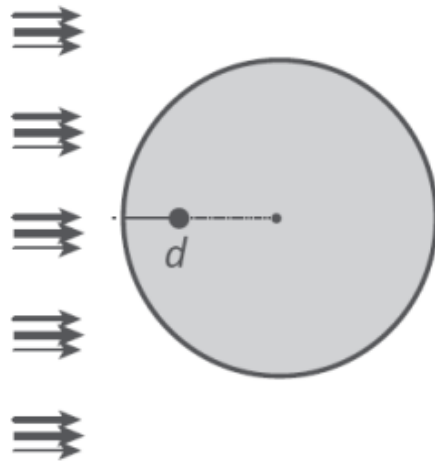


Figure 3.2: ICRU sphere in an aligned and expanded field. The point at which the ambient dose equivalent $H^*(d)$ is determined is located at depth d within the sphere along the radius of the sphere opposite to the alignment direction of the field [26].

The recommended value for the depth d is 10 mm. Since by definition $H^*(10)$ does not depend on the direction of the incident radiation, the instruments used to measure this quantity must also have a response that is as independent

as possible of the orientation in the radiation field. Any detector has a more isotropic response the higher the energy of the radiation. Therefore, the use of $H^*(10)$ is limited to highly penetrating radiations. The ambient dose equivalent is a quantity that, by definition, is measured in Sv and provides a reasonable estimate of the effective dose, E , which is the quantity used to express dose limits in radiation protection.

In the case of area monitoring in a weakly penetrating radiation field, the reference dosimetric quantity is the *directional dose equivalent*, $H'(d, \Omega)$. It is defined as the dose equivalent that would be produced by the corresponding expanded field in the ICRU sphere at depth d on a radius of the sphere located in a specified direction Ω . The recommended value for the depth d is $d = 0.07$ mm if $H'(d, \Omega)$ is referred to the skin, and $d = 3$ mm if $H'(d, \Omega)$ is referred to the eye. Since, by definition, the directional dose equivalent depends on the direction of the incident radiation, the instruments used to measure this quantity must also have a response that is as dependent as possible on the orientation in the radiation field. On the other hand, any detector has a response that is less isotropic the lower the energy of the radiation.

Individual monitoring in radiation protection involves dosimetric measurements carried out in environments where individuals may be exposed to ionizing radiation fields. Just like in area monitoring, the purpose of individual monitoring is to provide basic quantitative data to estimate the values of the protective quantities H_T or E for individuals exposed to that radiation field. Unlike area monitoring, in individual monitoring radiation measurement instruments are worn by individual persons and detect the same radiation field to which the person is exposed.

The dosimetric quantity used for individual monitoring, the *personal dose equivalent*, $H_p(d)$, is defined as the dose equivalent in soft tissue at a point at

depth d in the human body. The quantity $H_p(d)$, measured in Sv, is used for monitoring both in highly penetrating and weakly penetrating radiation fields, with d set at either 10 mm or 0.07 mm, respectively. For the calculation of $H_p(d)$ values, special anthropomorphic phantoms (made of tissue-equivalent material) descriptive of the body parts of interest are used, as shown in **Figure 3.3**.

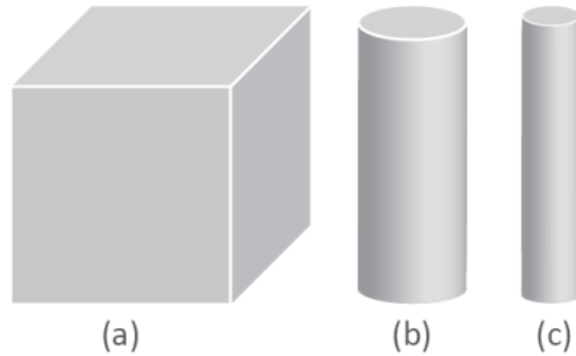


Figure 3.3: Examples of phantoms (a, b, c) made of tissue-equivalent material with different shapes for the calibration of dosimeters in terms of personal dose equivalent $H_p(d)$ [26].

3.2. Dosimetry at Laser Facilities

Dosimetry, in the context of a laser-generated radiation fields, is notably complex due to several specific challenges. The primary difference with respect to most facilities lies in the pulsed nature of the radiation field, where high dose-rates are delivered in discrete bursts that last very short periods (fs). This difference poses a significant challenge for active dosimetry, which aims to provide real-time measurement. High dose-rates and high repetition rates of the discrete bursts can lead to saturation effects or pile-up effects on the dosimetry devices, as will be discussed further in the following sections.

The complexity is further compounded by the diverse nature of the radiation field, which can comprise various radiation types and energies. The usual purpose of these experiments is to accelerate a specific type of particle; however, due to the nature of the process, various types of particles are produced and accelerated. Moreover, these accelerated particles create secondary radiation through collisions with the surrounding material (such as target, equipment, air). These factors increase the complexity of dosimetry in laser-driven accelerators, necessitating the use of devices tailored for this application. In fact, the adopted detector should be able to efficiently measure the dose from a radiation field with a wide energy spectrum and various types of radiation.

Additionally, the interaction of subnanosecond laser pulses with solid targets generates strong electromagnetic pulses (EMPs) [31] that have the potential to damage electronic devices. This necessitates additional protective measures and imposes constraints on the setup of detection instrumentation, since traditional dosimeters are not designed to sustain strong EMPs. These topics will be further detailed in the subsequent sections.

3.2.1. Timing of the dose delivery

One of the most notable characteristics of the radiation fields expected at laser-driven accelerator facilities is their pulsed temporal profile. A pulsed radiation field can be described as a field with radiation delivered in discrete bursts (or pulses), rather than continuous.

When the laser beam interacts with the primary target, it generates accelerated particles, such as electrons, protons, or heavy ions, depending on the specific target and accelerator mechanism. Multi-terawatt to petawatt

class lasers typically exhibit pulse durations ranging from tens to hundreds of femtoseconds. The accelerated particles beam, resulting from the laser-plasma interaction in the case of LWFA, can interact with the surrounding equipment, producing secondary radiation. The timescale for the delivery of this secondary radiation can be several orders of magnitude longer than that of the initial pulse.

For instance, the time dynamics of dose deposition by electron beams striking a cylindrical water phantom ($R = 20$ cm, $Z = 30$ cm) has been studied using FLUKA Monte Carlo simulation by Horvath and others [32]. The results for 50 MeV electron beams (within the energy range found at the ALFA experimental station at ELI Beamlines) are shown in **Figure 3.4**. It is observed that the time required to achieve 99% dose deposition is on the order of hundreds of picoseconds, representing a significant difference of two to three orders of magnitude from the initial laser pulse duration (< 30 fs).

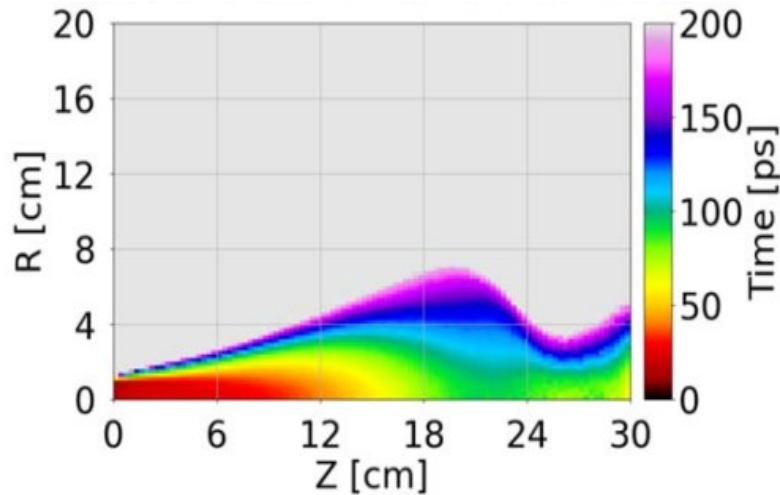


Figure 3.4: Time required to deposit 99% of the total dose. The scoring bin size is 2 mm (radial) \times 3 mm (longitudinal). Time scoring is done with 400 fs time bins [32].

The temporal spreading of dose delivery compared to the initial pulse is beneficial as it reduces the dose-rate by partially distributing the total dose over a longer period. This is crucial for real-time dose recording using active detectors, which typically operate in pulse mode. In pulse mode, the measurement equipment is designed to register each individual radiation quantum interacting with the detector [33]. Pulse mode operation offers significant advantages in sensitivity and the ability to measure the energy of the incident radiation, as the amplitude of the pulse signal produced in the detector is proportional to the particle's energy (with certain considerations depending on the specific detector, as discussed in [33]).

Many dosimeters operate in pulse mode because the dose can be easily determined based on the particle's energy using tabulated conversion coefficients. However, detectors working in pulse mode are subject to the so-called *dead time* effect. Dead time refers to the minimum time interval required by the detector to distinguish two consecutive events as separate rather than a single event. As a result of two particles impinging on a time interval shorter than the dead time, only one event or none may be recorded, leading to signal loss. In Chapter 5, a more in-depth discussion of dosimetry instrumentation in the context of accelerators, particularly electron laser-driven accelerators, will be provided, outlining potential solutions to address this issue.

It is important to note that the signal collection time in numerous detectors operating in pulse mode is typically on the order of microseconds. This means that, despite the extended timing of dose deposition mentioned earlier, which occurs on the picosecond timescale, this timeframe is still many orders of magnitude smaller than the timescales at which detectors in pulse mode efficiently operate. Hence, a significant loss of signal and subsequent

underestimation of the dose are likely to occur when conducting dosimetry at a laser-driven accelerator facilities using standard dosimeters not explicitly tailored for pulsed fields.

An evaluation involving 29 instruments, comprising 14 area monitors and 15 active personal dosimeters, was conducted at the Helmholtz-Zentrum Berlin für Materialien und Energie GmbH by Caresana and others [34]. The study utilized a cyclotron that generated a 68 MeV proton beam directed at a 20 mm thick tungsten target, resulting in a pulsed neutron field with a burst duration ranging from 1 to 40 μ s, a repetition rate set at 100 Hz and varying beam current (thus altering the dose yield per burst). The findings indicate that the response of all standard rem-counters deviates from linearity within the 1-10 nSv per burst range. Conversely, instruments specifically engineered for pulsed fields, such as the LUPIN BF-3 [35] area monitor (to be elaborated on in Chapter 5), demonstrate a linear response even at high dose-rate levels exceeding 100 nSv per burst. In pulsed radiation fields characterized by shorter pulse durations, such as those found in LWFA facilities, it is expected that the dosimeters employed will exhibit underestimation rates that are at least equal to, if not greater than, those observed in this study.

3.2.2. Source term

In the context of laser-driven electron accelerators, when the accelerated electron beam interacts with thick targets (i.e., surrounding equipments), it gives rise to electromagnetic cascades. This means that the energy range of the produced particles broadens up dramatically, through bremsstrahlung radiation, photoelectric absorption, couple production, Compton scattering and others interaction mechanisms.

Additionally, the presence of high-energy photons that are generated in the interaction process leads to the production of neutrons through various photonuclear reactions, as elaborated by Swanson [36,37]. The total photonuclear reaction production is determined by integrating the cross-section of photonuclear reactions and multiplying it by the track length distribution of the photons produced in the electromagnetic cascade. The outcomes for different materials are illustrated in **Figure 3.4**. Other production mechanisms become relevant in the case of photon production with energies exceeding 150 MeV in the electromagnetic cascade; however, these are not of interest in the current study due to the lower energies involved.

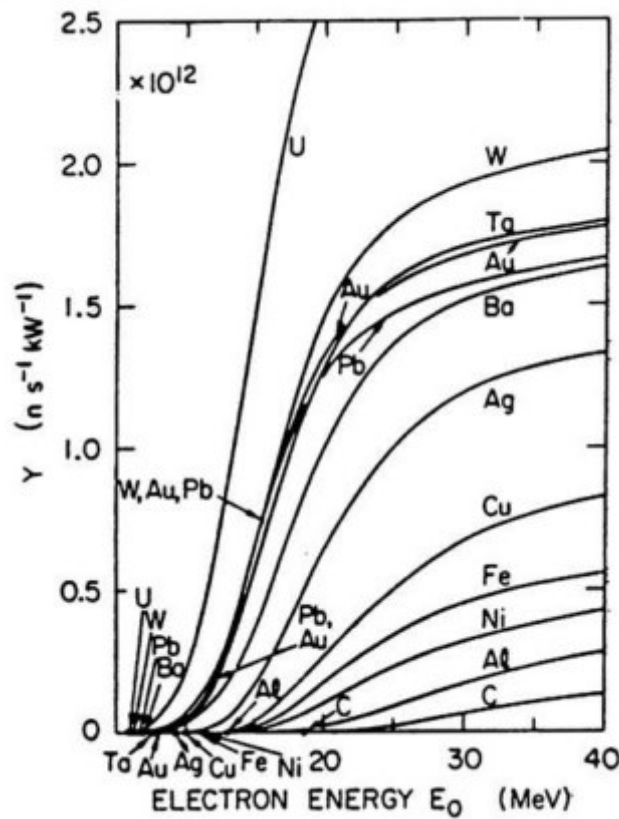


Figure 3.4: Fraction of photonuclear reactions produced in the electromagnetic cascades initiated by an incident electron on thick targets per unit of beam power, as a function of the energy of the electron [36].

3.2.3. Electromagnetic Pulses

When a laser pulse interacts with a target, it generates electromagnetic pulses (EMPs) whose fields are proportional to both the laser intensity and energy. The development of chirped pulse amplification and the rapid advancement of sub-picosecond laser systems have been shown to produce intense EMPs, which can pose a threat to electronics and computers [31].

Electromagnetic emissions are produced at all stages of the laser–target interaction, with two main phenomena generating microwaves in distinct frequency domains. The first phenomenon is associated with electron ejection from the target, leading to the creation of a return current due to charge imbalance. This results in EMPs in the terahertz (THz) domain, which are particularly harmful to electronic circuits. The second mechanism of microwave generation involves the relaxation of accumulated charge on the target during the laser pulse interaction, operating in the gigahertz (GHz) domain [31].

Considering that modern electronic hardware and communication equipment operate in the frequency domain of tens of GHz, they are particularly sensible to these type of emissions. Dosimeters and the related electronics are susceptible to EMPs, since they are not tailored to work in such an environment, too. As a result, countermeasures are required to protect the equipment and ensure its proper functioning throughout the entire data taking campaign. Among all countermeasures, one of the most common and successful is to put the device in a Faraday cage. A Faraday cage is simply an enclosure made of conductive materials that blocks external electric fields and electromagnetic radiation. It works by redistributing electric charges on its surface to cancel out external fields, creating a shielded environment inside. However, the complexity of modern hardware, like cameras and fast

oscilloscopes, makes it hard to predict the actual sensitivity to a certain EMP field, which usually spans multiple bands on different timescales. As a consequence, tailored shielding techniques may be required depending on the specific setup [31].

For instance, detailed studies have been carried out in the design of the ELI Beamlines facility by Weber and others [38] to address the risk posed by intense EMPs generated by the L4 laser system, which delivers pulses with energy exceeding 1.5 kJ, peak power of 10 PW, and duration of 150 fs. Significant efforts were made to protect against EMPs, including shielding laboratories with dense structural grids and robust ceilings, floors, and walls, in accordance with EMP protection standards.

However, further simulations using the High-Frequency Structure Simulator in the ANSYS software package revealed that a considerable amount of pulse energy transfers from the interaction chamber to the compressor chamber, with some EMP escaping from the vacuum assembly. To address these EMP effects, strategies involving blocking and absorption were explored. Initial tests on selected materials were conducted, and ongoing work includes optimizing the absorbing structure for vacuum vessels.

4. Monte Carlo as a Tool for Dosimetry

4.1. Monte Carlo Overview

The Monte Carlo simulation (MCS) method is a powerful modelling tool for the analysis of complex systems. It may be generally defined as a methodology for obtaining estimates of the solution of mathematical problems by means of random numbers [39]. The model was developed in the 1940s by Ulam and others specifically to address physical problems where analytical approaches are not viable due to the complexity of the system [40]. This was the case of neutron propagation in the context of the Manhattan Project, the American World War II effort to develop nuclear weapons.

4.1.1. The Method

The method can be illustrated with a practical example: the problem that led to the development of the method itself. Consider a medium in which a nuclear particle is introduced, capable of producing other nuclear particles with specific distributions in energy and direction. The capability of these particles to generate additional particles depends on their position within the medium and on their energy. Consequently, the behavior of such a system can be described by a set of integro-differential equations, known in the kinetic theory of gases as the Boltzmann equations. Classical methods for addressing this problem are

extremely labor-intensive and can provide analytical solutions only for the simplest systems. The idea is to tackle the problem using a statistical approach: a finite number of particles is described by a set of parameters defining their velocity, energy, position and so on. It is assumed that the probability distribution for each process that a single particle can undergo in the system (i.e., scattering direction probability distribution, decay probability distribution, etc.) is known. Random processes are initiated, leading after a specified time interval to the determination of a new set of values for each initial particle. This procedure is repeated as many times as required for the duration of the real process. The result is a sample of the set of all possible chains of events and it better represents the real evolution of the system as the initial sample of particles increases [40]. The essential feature of this process is that it avoids the multiple integrations or multiplications of the probability matrices, resulting in much shorter computational times.

The MCS method is particularly well fitting with the calculation capabilities of the modern computers. Indeed, its success and widespread diffusion coincided with the incredible development these machines saw in the last decades. Specifically, the operations to be carried out by the machine are of two classes: production of random variables with their probability frequency distribution (PDF) equal to those which govern the change of each parameter; calculation of the values of those parameters which are deterministic (i.e., obtained algebraically from the others).

4.1.2. Pseudo-Random Numbers

The production of random variables is a crucial point of the method since it must ensure the stochasticity of the input variables and at the same time follow the PDF of the designated phenomenon. This task can be achieved with

different approaches, depending on the data available and on the scope of the simulation. The common denominator of all the approaches is the fact that a sequence of random numbers is required as initial input. This task has represented, and still represents, an important topic subject of active research. In 1956 Von Neumann proposed to have the computer directly generate the ‘random’ numbers by means of an algorithm [39]. In this case it is more accurate to talk about ‘pseudo-random numbers’, since their generation is deterministic and the same exact sequence can be extract starting from the same initial input. This initial input is called ‘seed’ and its existence is important for the reproducibility of the simulation.

4.1.3. Inverse Transform Method

Afterwards, it is necessary to correlate the uniformly distributed random numbers to the desired PDF. Assuming to know the function f describing the PDF from which the random variables are to be generated, the most direct approach is the *inverse transformation method*, which can be summarized as follows. Let $X \in (-\infty, +\infty)$ be a random variable with a PDF $f_X(x)$. Then the cumulative density function (CDF) is defined as:

$$F_X(x) = \int_{-\infty}^x f_X(x') dx' = P(X \leq x)$$

Where $P(X \leq x)$ represents the probability that the random variable X is lower than x , an arbitrary value. Since from the definition $F_X(x)$ is a non-decreasing function, for any $y \in [0, 1)$ its inverse may be defined as:

$$F_X^{-1}(y) = \inf\{x : F_X(x) \geq y\}$$

It is always possible to obtain values of X following the CDF $F_X(x)$ starting from values R sampled from the uniform distribution $U_R[0, 1)$. It is therefore clear that:

$$P(R \leq r) = U_R(r) = r$$

Where R is the random variable extracted from the uniform distribution and r is an arbitrary parameter. From the following relation it is possible to calculate the random variable $X = F_X^{-1}(R)$:

$$P(X \leq x) = P(F_X^{-1}(R) \leq x)$$

Remembering that F_X is an increasing function and applying it to both sides of the inequality on the right hand side:

$$P(X \leq x) = P(R \leq F_X(x)) = F_X(x)$$

It follows that $X = F_X^{-1}(R)$ is extracted from $F_X(x)$. These relationships are well illustrated in **Figure 4.1**.

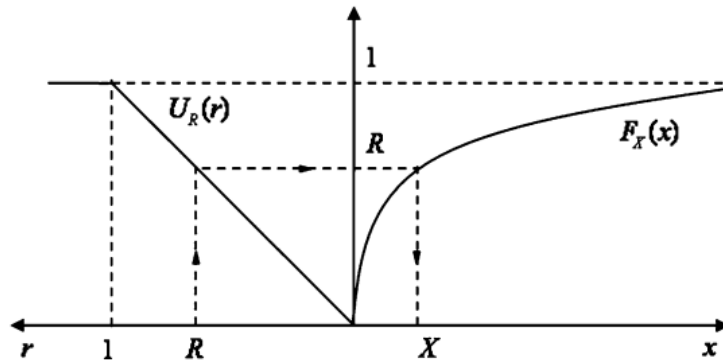


Figure 4.1: Inverse transform method for continuous distributions. It is clear from the figure that $P(X < x) = P(R < r)$, relation that can be retrieved from $P(X \leq x) = P(R \leq F_X(x))$ and $F_X(x) = r$ [39].

It is common for the cumulative distribution function to be analytically non-invertible, making it impossible to express X as a function of R . In such cases,

a frequently used approximate method involves interpolating $F_X(x)$ with a polygonal function and then performing the inversion this approximation.

4.1.4. Convergence of the Method

The objective of a Monte Carlo simulation is to determine an output value Ω for the system being analyzed. By conducting a cycle of N simulations, we obtain N random variables X_i , each of which has Ω as its expected value. Consequently, the arithmetic mean \bar{X} of the N random variables derived from the simulations can be used as an estimator for Ω .

$$\bar{X} = \frac{\sum_{i=1}^N X_i}{N}$$

Each one of these random variables X_i will have an expected value $E[X_i] = \Omega$ and a variance $Var[X_i] = \sigma^2$. Therefore, the expected value and the variance of the arithmetic mean are:

$$E[\bar{X}] = E\left[\frac{\sum_{i=1}^N X_i}{N}\right] = \frac{\sum_{i=1}^N E[X_i]}{N} = \Omega$$

$$Var[\bar{X}] = E\left[(\bar{X} - \Omega)^2\right] = Var\left[\frac{\sum_{i=1}^N X_i}{N}\right] = \frac{\sum_{i=1}^N Var[X_i]}{N^2} = \frac{\sigma^2}{N}$$

By setting a tolerance level and estimating σ^2 , it becomes possible to determine the number of simulations N required to achieve the desired sensitivity of the estimator \bar{X} . However, it is important to note that as the number of simulations increases the computational time for the simulation cycle will also rise correspondingly. Therefore, it is essential to find a balance between the sensitivity of the estimator and the computational time.

4.2. MCS in Dosimetry

The application of the Monte Carlo method in dosimetry has grown drastically since the 1970s [41]. MC applications range from calculating fundamental dosimetric quantities to simulating radiotherapy treatment planning. Over time the MC codes developed for the purpose of high energy physics, were extended and exploited also in the field of nuclear medicine, radiology, radiation therapy [42,43]. In this work the FLUKA code in its version 4.0 and with the aid of the FLAIR interface has been adopted.

4.2.1. FLUKA

FLUktuierende KAskade (FLUKA) is a Monte Carlo simulation code developed in the FORmula TRANslator (FORTRAN) programming language [44]. Its development was a collaborative effort between the European Laboratory for Particle Physics (CERN) and the Italian Institute for Nuclear Physics (INFN) from 2002 to 2019, after which the code continued to evolve independently. The version of FLUKA utilized in this study is FLUKA4-4.0, which is distributed by CERN.

FLUKA has a wide range of applications and was specifically designed to simulate, with high accuracy, the interaction and propagation of approximately 60 types of particles, including photons and electrons, as well as their corresponding antiparticles. It allows for the evaluation of proton-proton interactions and heavy ion collisions over a wide range of energies within the same simulation. It also takes into account hadronic and electromagnetic cascades initiated by secondary particles. These features make it particularly suitable for radioprotection purposes, such as studying induced radioactivity, the production of radionuclides, and the transport of residual radiation.

FLAIR (Fluka Advanced Interface) is a graphical interface developed to simplify the use of the code [45]. It allows users to modify routines, execute codes, visualize geometry in real time, and view and read output files. To modify the input file, users can introduce the desired commands and functions by adding what are referred to as "CARDS" in the "Input" section of the interface. A representative screenshot of this section is shown in **Figure 4.2**.

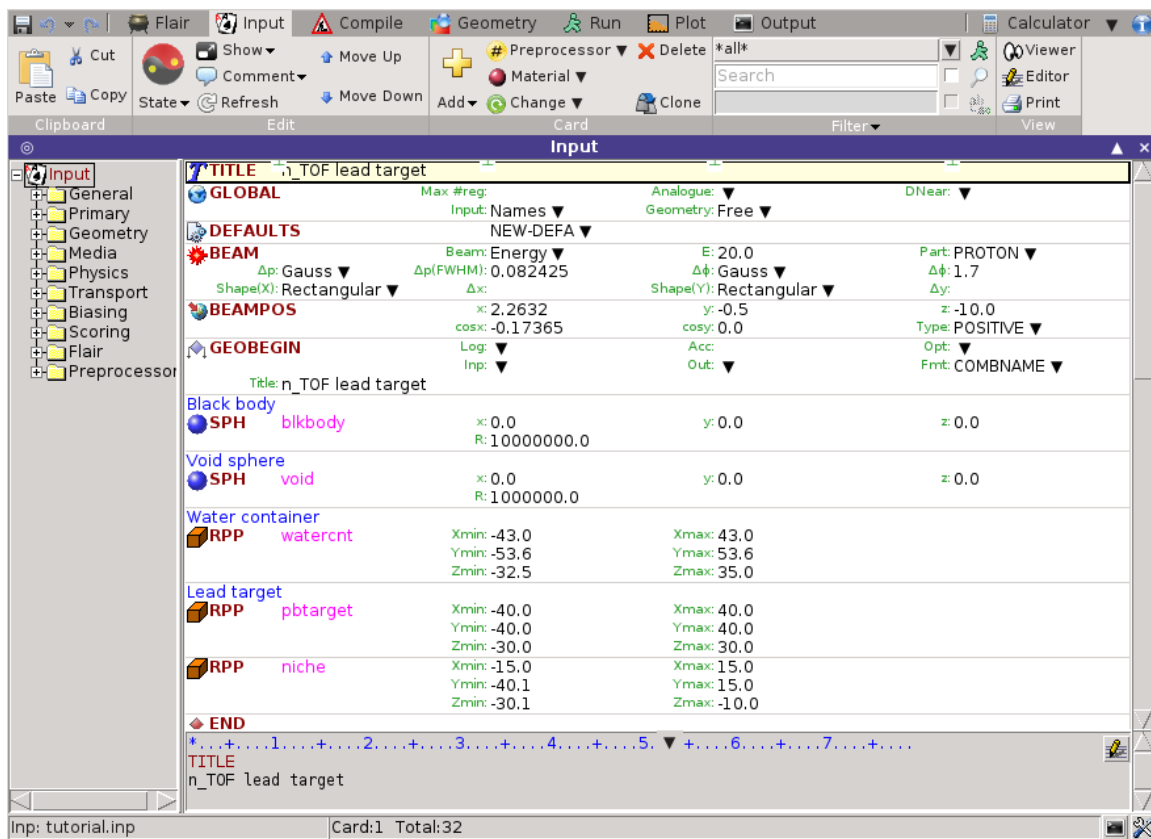


Figure 4.2: Screenshot of the Input section of the FLAIR interface for FLUKA. On the left the characteristic “tree” structure of the file is shown, while on the main window all the CARDS and their respective parameter are displayed [from: <https://www.fluka.org/flair/ss-input.html>].

4.3. MCS with FLUKA at Laser Facilities

The FLUKA code is a widely used tool within many research centers worldwide [46,47,48,49]. For instance, it serves as the primary tool for all beam-accelerator calculations at CERN [50], in addition to numerous calculations tailored to specific experiments within the accelerator complex. FLUKA simulations are also routinely utilized in various areas, including secondary beam design, energy deposition, radiation damage, shielding activation, residual dose rates, and waste disposal [51]. These applications necessitate that the physics models remain reliable across a broad energy range, encompassing all elementary particle and ion beams, including those up to uranium. Consequently, the code is utilized globally for radioprotection calculations at accelerator facilities and at laser facilities, being one of the few that covers the necessary energy range [52].

For instance, the FLUKA code has been employed by Olšovcová and others [53] for the assessment of the radiological hazard in the proximity of a TW-class laser system. Radioprotection studies have also been conducted using FLUKA at the Swiss Free Electron Laser facility (Paul Scherrer Institute) [54] and for the 2.5 PW ultrashort laser at the Munich Centre for Advanced Laser Applications facility [55], among others.

5. Dosimetry Study at ALFA

5.1. Purpose and Outline of the Study

As detailed in Chapter 3, laser-driven accelerator facilities represent a very unique and challenging environment for dosimetry. Many dosimeters are not specifically designed to operate in pulsed fields, and none are explicitly designed for the pulsed fields encountered within this particular time range. Furthermore, even those dosimeters that are intended for use in pulsed field environments may yield inaccurate results due to the ultra-short timing of dose delivery. This issue is particularly relevant at the ALFA experimental station, where the femtosecond laser-driven wakefield acceleration generates ultra-short electron bunches. The secondary radiation field produced by the interaction of the primary electrons with the surrounding materials delivers high doses on the order of picoseconds (see Paragraph 3.2.1), posing challenges even for the most advanced dose-rate monitors.

Conversely, verifying measurements using Monte Carlo simulations is also not a straightforward task. This complexity arises from the significant uncertainties that result from frequent changes in both the parameters of the primary beam and the experimental setup in laser experiments and, particularly in the context of ALFA [25]. Parameters of the primary beam that may change include the maximum energy and its spread, and the spatial distribution. Changes on the experimental setup may involve different types of collimators, thin or thick targets positioned at arbitrary distances from the

source and diagnostic instrumentation (i.e., spectroscopy equipment, calorimeters).

Despite significant advancements in the development of tailored devices for accurate dosimetry in ultra-short laser facilities [35,56,57], along with comparative studies addressing the response of existing dose monitors [35,58], the body of literature addressing these topics is still limited.

This work specifically aims to address these challenges, by characterizing the secondary radiation emitted by ALFA while simultaneously studying the response of various dosimeters. This task is particularly complex, as accurate data analysis, supported by physical considerations, is necessary to identify the limitations of each detector and to determine where they accurately measure the dose rate. Additionally, discrepancies among the detectors must be explained, and the causes of any misdetections identified. Moreover, a comparison with a Monte Carlo simulation should be used to benchmark the experimental results.

This chapter provides an overview of the materials and methods employed in this study. First, a comprehensive description of the selected dosimeters and their characteristics is presented. Next, the setup of the experimental line and its components is detailed. Finally, the parameters used for the Monte Carlo simulations are outlined.

In the subsequent chapter, the measurements obtained during the data collection campaign at ALFA are analyzed, and a thorough description of the results is provided. Discrepancies observed between the data recorded by different dosimeters are discussed, with the aim of identifying factors that may contribute to inaccurate results. This analysis is conducted through both physical and technical considerations, as well as through Monte Carlo simulations of the irradiation process at ALFA.

5.2. Dosimeters Setup

The ALFA experimental station has been outfitted with three active dosimeters that can record both the dose rate ($\mu\text{Sv/h}$) and the total dose (μSv). The adopted area monitors are:

- LUPIN BF3-NP (Else Nuclear)
- Nausicaa ICP-T-PF (Else Nuclear)
- LB6419 (Berthold Technologies)

The first device measures the dose-rate delivered by the neutrons only, while the second device measures the dose-rate from gamma radiation. The third device features two distinct and independent detection channels, enabling simultaneous measurement of both neutrons and gammas. Consequently, the selection of these three dosimeters facilitates a side-by-side comparison of both types of radiation, thus enhancing the understanding of the radiation field, which is not known in advance. Additionally, a comparison of their results provides insight into their behavior in an ultra-short pulsed radiation field. **Table 5.1** summarizes the main characteristics of the three dosimeters.

Dosimeter	Detection	Energy Range	Sensitivity	Dose-Rate Range
Lupin BF3-NP	Neutrons	0.025 eV – 10 GeV	0.6 cps/ $\mu\text{Sv/h}$	10 nSv/h – 100 mSv/h
Nausicaa ICP- T-PF	Gamma Part.	30 keV – 10 MeV	$2 \cdot 10^{-8}$ A/R/h	10 nSv/h – 100 mSv/h
LB6419	Neutrons & Gamma Part.	N.A.	N.A.	N.A.

Table 5.1: Main features of the utilized dosimeters.

5.2.1. LUPIN

The LUPIN (*Long interval Ultra-wide range dynamic, Pile-up free Neutron REM-counter*) BF₃-NP is a Radiation Environmental Monitor (REM) counter type instrument produced by ELSE Nuclear [59]. It is specifically designed to measure the ambient dose equivalent ($H^*(10)$, see **Chapter 3**) in pulsed environments. The LUPIN is equipped with a cylindrical BF₃ proportional counter (Centronics 15EB/20/25SS) with gas pressure of 26 kPa placed at the center of a cylindrical moderator [35], as shown in **Figure 5.1**. It is capable of detecting neutrons from thermal energies (i.e., 0.025 eV) up to 10 GeV, with an estimated sensitivity of 0.6 cps/ μ Sv/h (cps stands for counts per second). The dosimeter can measure an ambient dose equivalent, $H^*(10)$, ranging from 10 nSv/h to 100 mSv/h [60].

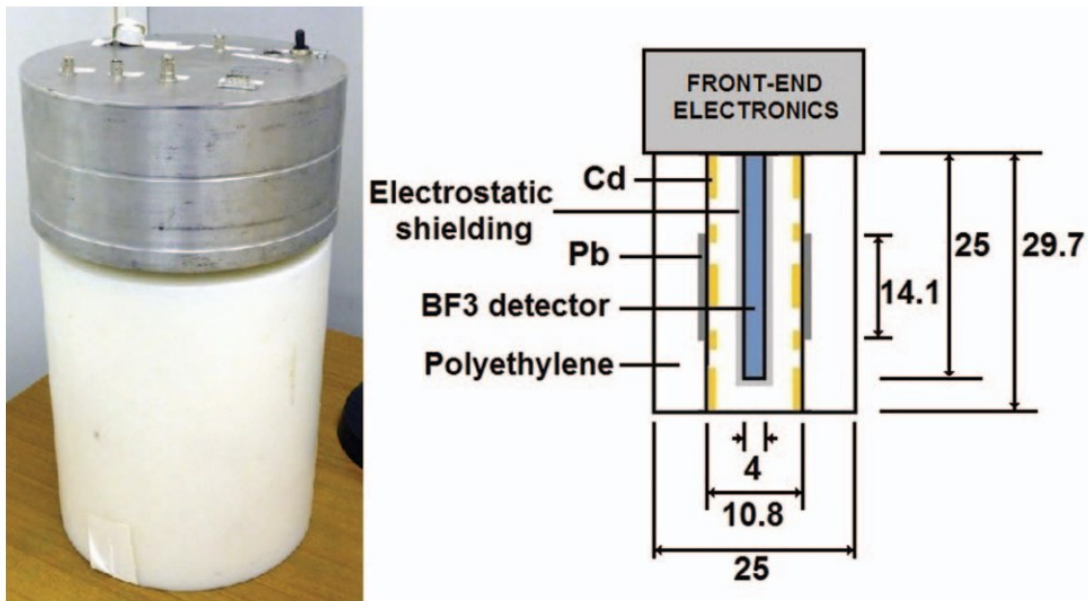


Figure 5.1: Photograph and scheme of the LUPIN area monitor (dimensions in centimeters) (from [35]).

To improve the response function, the moderator assembly of LUPIN is designed with a polyethylene layer that incorporates cadmium and lead

inserts. The cadmium inserts reduce sensitivity to thermal neutrons, while the lead inserts enhance sensitivity to high-energy neutrons by utilizing (n, xn) nuclear reactions.

Another key feature of LUPIN is its capability to function effectively in environments characterized by pulsed neutron radiation. Measurements taken in pulsed neutron fields have shown that the detector can withstand doses per pulse of up to 500 nSv, with only a 20% underestimation of the actual delivered dose [35].

Unlike traditional pulse acquisition techniques that suffer from dead time losses, the LUPIN operates in current mode. The current generated in the proportional counter is integrated over a fixed duration and divided by the mean collected charge (MCC). The MCC represents the charge produced by a single neutron interaction and is determined experimentally through irradiations at very low neutron fluence, as specified by the manufacturer. This approach yields a total count of neutron interactions over a specified time period, free from dead time losses. However, relying solely on current acquisition mode is insufficient, as secondary photons can also interact and generate charges in the proportional counter. If these charges were attributed to neutron interactions, it would lead to an inaccurate count of neutron interactions.

To address this issue, the LUPIN employs a technique known as the derivative method. The current signal produced in the proportional counter is differentiated, and a threshold is applied to the derivative of the signal, which is related to the LET of the impinging particle. Consequently, the derivative of a neutron-induced signal is greater than that of a photon-induced signal, even when multiple photons interact simultaneously. This principle allows for effective rejection of photon-induced signals.

5.2.2. Nausicaa

The Nausicaa ICP-T-PF is an ion chamber-based gamma radiation monitoring unit [61] produced by ELSE Nuclear [59]. The 10-liter ion chamber is filled with a mixture of Argon and Xenon at pressures of 8 and 2 atm, respectively. It is capable of detecting photons within the energy range of 30 keV to 10 MeV, with an estimated sensitivity of approximately $2 \cdot 10^{-8}$ A/R/h (where A denotes amperes, R represents roentgens -a unit of exposure to ionizing radiation- and h indicates hours). The measurement range for the standard version of the device extends from 10 nSv/h to 10 Sv/h, whereas the -PF (pulsed field) version, utilized in ALFA, has a measurement range from 10 nSv/h to 100 mSv/h. Although this latter version of the device shares the same detector characteristics (i.e., structure, filling gas, operating voltage) as the standard version, it is distinguished by front-end electronics and data collection software specifically designed for efficient operation in pulsed field environments [62]. The shorter measurement range, along with the different electronic hardware (a 7-decade electrometer compared to the 9-decade electrometer in the standard version), is required to manage higher dose-rates expected in a pulsed field environment.

5.2.3. Pandora

The LB6419, also known as “Pandora”, is an area dosimeter intended mainly for pulsed and continuous neutron and gamma radiation [58] developed by BERTHOLD Technologies [63], DESY [64] and STRUCK Innovative Systeme [65]. The instrument features two distinct and independent radiation detection channels: one for thermal neutron detection and another for gamma detection. The thermal neutron detector employs a ^3He proportional counter, which is surrounded by a polyethylene moderator with cadmium inserts to optimize the

energy-dependent response. The gamma detection channel consists of a plastic scintillator coupled with a compact, fast photomultiplier that offers a wide dynamic range.

The detector is designed to mitigate the effects of dead time that typically impact detectors operating in pulsed field environments by utilizing the activation of short-lived nuclides. To achieve this, the dosimeter incorporates a carbon layer within the conventional moderator material necessary for the thermalization of high-energy neutrons. Upon interaction with a burst of neutrons, this carbon layer activates the material through the reactions detailed in **Table 5.2**. The decay products of these intermediate short-lived states are subsequently detected using time-resolved readout and identified by analyzing their timing characteristics.

The system includes power supplies, analog electronics, and a fast analog-to-digital converter readout and analysis module that records pulse heights along with time stamps, all housed within an electronic enclosure.

Nuclear Reaction	Decay Pattern	Half-Life	Energy Threshold
$^{12}\text{C}(n, p)^{12}\text{B}$	$^{12}\text{B} \rightarrow ^{12}\text{C} + \beta^- + \nu$	20 ms	14 MeV
$^{12}\text{C}(n, p\alpha)^8\text{Li}$	$^8\text{Li} \rightarrow \alpha + \alpha + \beta^- + \nu$	840 ms	20 MeV
$^{12}\text{C}(n, X)^9\text{Li}$	$^9\text{Li} \rightarrow ^9\text{Be}^* + \beta^- + \nu$ $^9\text{Be}^* \rightarrow \alpha + \alpha + n$	178 ms	40 MeV

Table 5.2: Nuclear reactions with carbon as target material used in the LB 6419 (adapted from [57] and [66]).

However, some limitations of this area monitor include the fact that the activation mechanism employed to overcome the dead time effect becomes effective only for neutrons with energies above the threshold listed in **Table 5.2**. Moreover, the use of ^8Li , with a half-life of 840 ms, limits the range of the pulse frequency over which it can be used [66]. Measurements conducted at the HZB in pulsed radiation fields with a repetition rate of 100 Hz [35] (see Paragraph 3.2) highlighted considerable underestimation when the dose exceeded 50 nSv per burst, as shown in **Figure 5.3**.

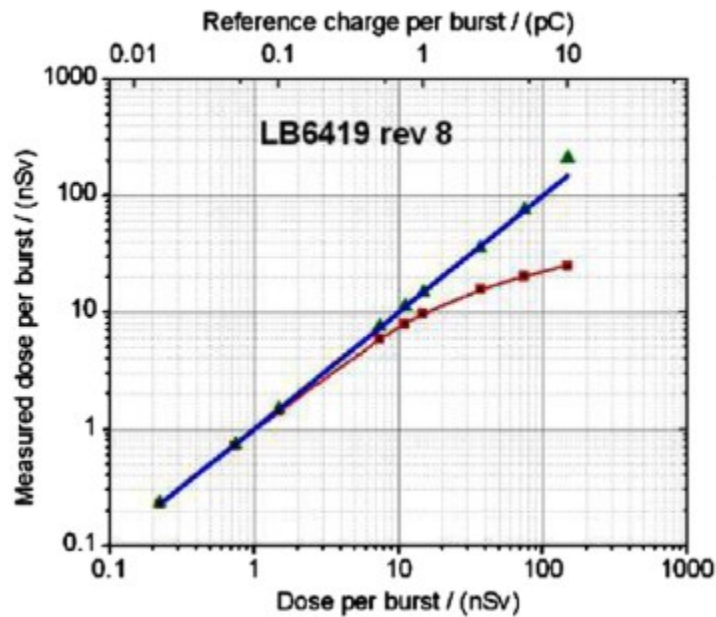


Figure 5.3: Instrument linearity. The top x-axis reports the reference burst charge while the bottom x-axis reports the reference burst charge multiplied by the burst yield for the given instrument. The straight line is the bisector of the first quadrant, representing the ideal linearity. The square points are the raw instrument reading and the triangular points are the instrument reading corrected with the saturation correction formula (see [35]).

5.3. ALFA Setup

The configuration of the ALFA vacuum chamber was as follows: a slit and a 0.1 T dipole magnet were positioned approximately 51 cm and 58 cm from the source, respectively. A Lanex screen was mounted at the viewport for spectroscopy purposes, located at a distance of 102 cm from the source. A picture of the ALFA setup is shown in **Figure 5.4**, and a representation of the CAD drawing of the ALFA vacuum chamber is provided in **Figure 5.5**. The viewport flange utilized, which is not represented in the CAD drawing, was the Lesker VPZL-160, featuring a diameter of 160 mm [67].

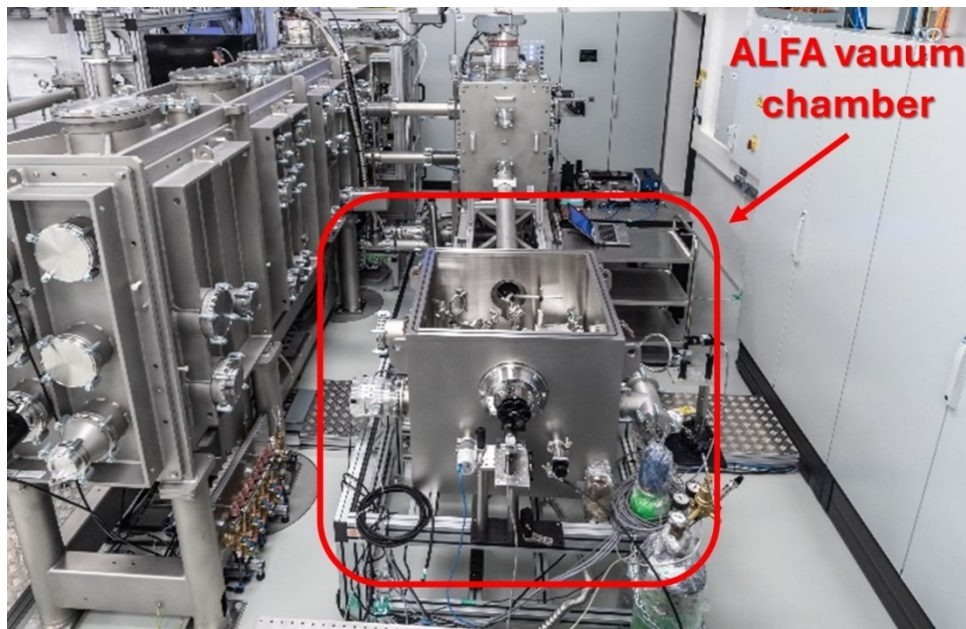


Figure 5.4: Image of a portion of the ALFA experimental hall. The ALFA vacuum chamber is highlighted within the red rectangle. At the time the picture was taken, the ceiling of the chamber had been removed, and the flange depicted differs from the one referenced in this work.

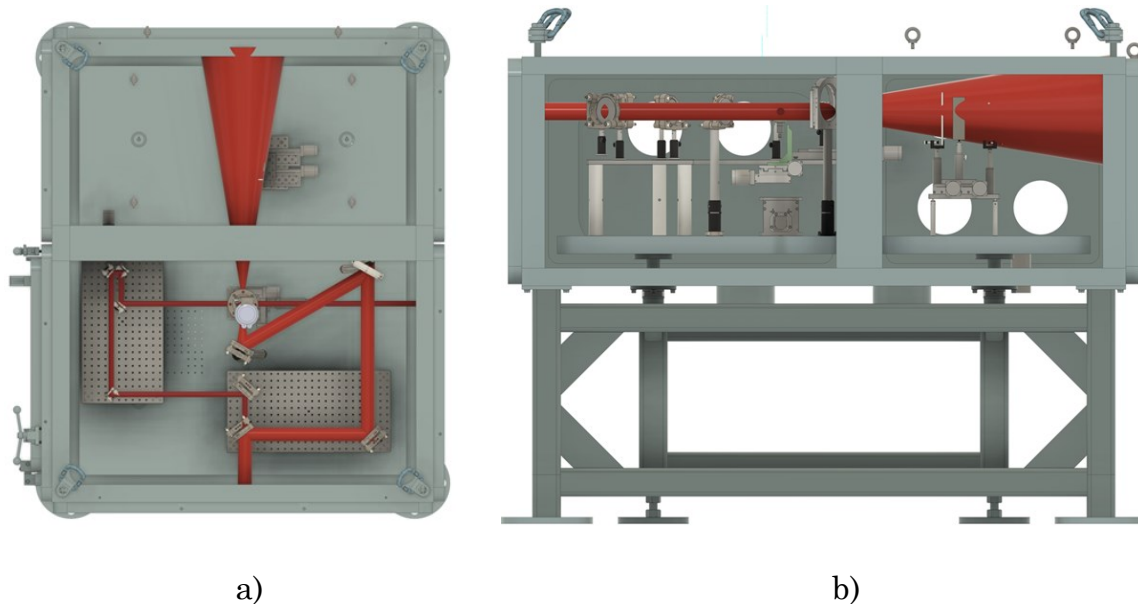


Figure 5.5: CAD drawing of the ALFA vacuum chamber and its components. Top (a) and side (b) view.

The detectors have been arranged on a table at an approximate height of 116 cm, positioned side by side. A beam dump, consisting of a 50 cm thick granite slab and a 10 cm thick lead slab, is also present to shield radiation from the corridor located behind it. The table supporting the detectors is situated 7 meters from the source and at an angle of approximately 30 degrees relative to the beam axis, adjacent to the beam dump, as schematically illustrated in **Figure 5.6**. A photograph of the detector setup in proximity to the beam dump is also presented in **Figure 5.7**. Furthermore, two additional Pandora detectors have been placed within the experimental hall to collect supplementary data: one located in the west corridor, directly behind the beam dump, and the other situated in the control room (refer to Figure 5.6).

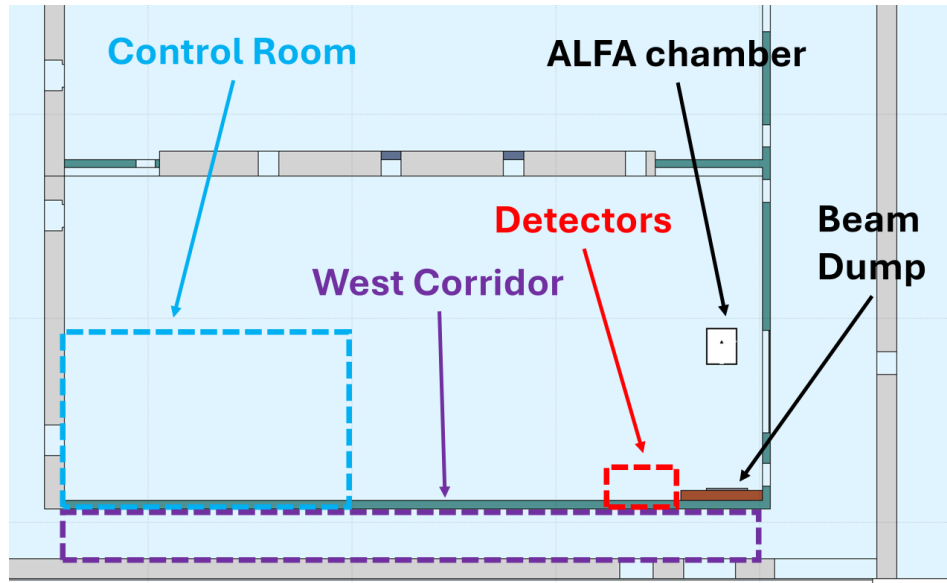


Figure 5.6: Top view of the FLUKA geometry model of the ALFA experimental hall. On the right, the ALFA chamber and the beam dump, which consists of granite and a lead slab, are visible. Dashed colored boxes delineate significant areas of the model. Specifically, the control room is highlighted in blue, the area containing the three dosimeters is marked in red, and the west-corridor is indicated in green.

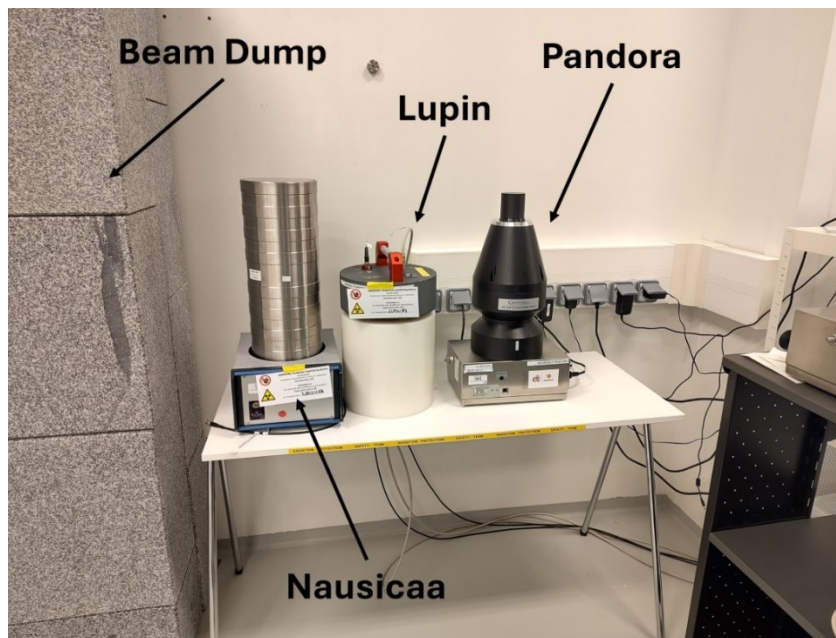


Figure 5.7: Setup of dosimeters for the measurement campaign in the ALFA experimental hall.

5.4. Monte Carlo Simulation Setup

5.4.1. Geometry

The Monte Carlo Simulation (MCS) has been carried out using the FLUKA code (version FLUKA4-4.0) and the FLAIR interface (see Chapter 3). The geometry of the laser building was already available and has been coded by the Monte Carlo Working Group in ELI Beamlines [68] for radiation protection studies. This geometry has been complemented by details about the specific setup of the ALFA experimental line and the ALFA vacuum chamber. A view of the FLUKA geometry of the ALFA experimental hall coded for the MCS can be seen in **Figure 5.8**. A close-up of the vacuum chamber and its component is displayed in **Figure 5.9**.

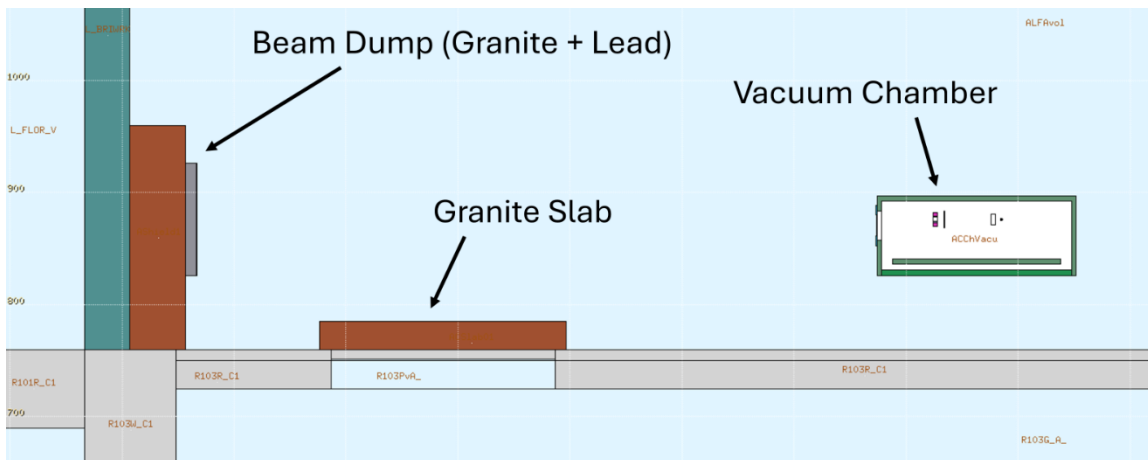


Figure 5.8: FLUKA geometry model of a portion of the ALFA experimental station, side view. From left to right, the model includes: the wall separating the experimental hall from the corridor, the beam dump composed of granite and lead slabs, a horizontal granite slab implemented for radiation protection purposes (i.e., to shield the underlying aperture), and the vacuum chamber where the source is located. Each square of the grid has a side length of 1 m.

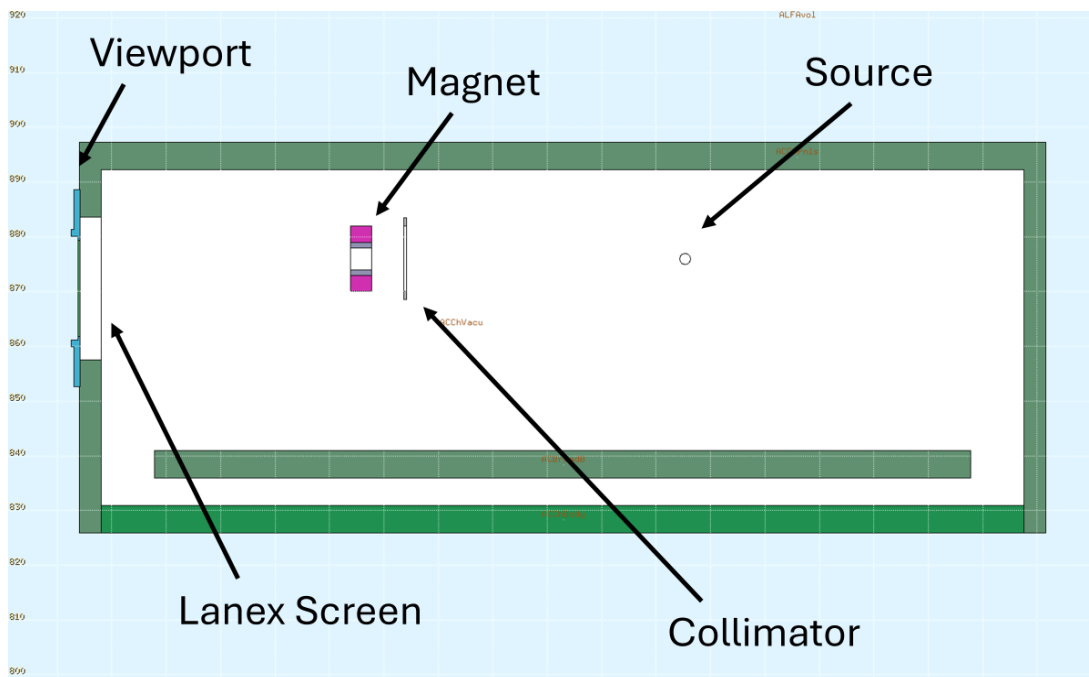


Figure 5.9: FLUKA geometry model of the ALFA vacuum chamber and its components, side view. Each square of the grid has a side length of 10 cm.

5.4.2. Source and Run

The source term has three components: the Quasi-Mono-Energetic (QME) electron beam; the low energy electron beam; the photon beam. The details of each component can be seen in **Table 5.3**. The source characteristics have been coded through a source subroutine (see Paragraph 4.2.1) and the simulation has been ultimately run with 10^5 primaries. A plot of the source spectrum employed in the MCS can be seen in **Figure 5.10**.

Beam Component	No. of Primaries/ Charge	Source Size	Energy Spectrum	Angular Distribution
QME electron beam	10 fC/shot	Pointlike	50 MeV Gaussian; 10 MeV FWHM	2.1 +/- 0.8 mrad divergence 7 mrad pointing uncertainty; flat angular distribution
Low-energy background electron beam	300 fC/shot	Pointlike	Flat distribution between 0 and 20 MeV	10 mrad divergence; 10 mrad pointing uncertainty flat angular distribution
Photon beam	$10^9 - 10^{10}$ photons/shot	Pointlike	80 keV Gaussian; 16 keV FWHM	10 mrad divergence; 10 mrad pointing uncertainty flat angular distribution

Table 5.3: Characteristics of the source term components.

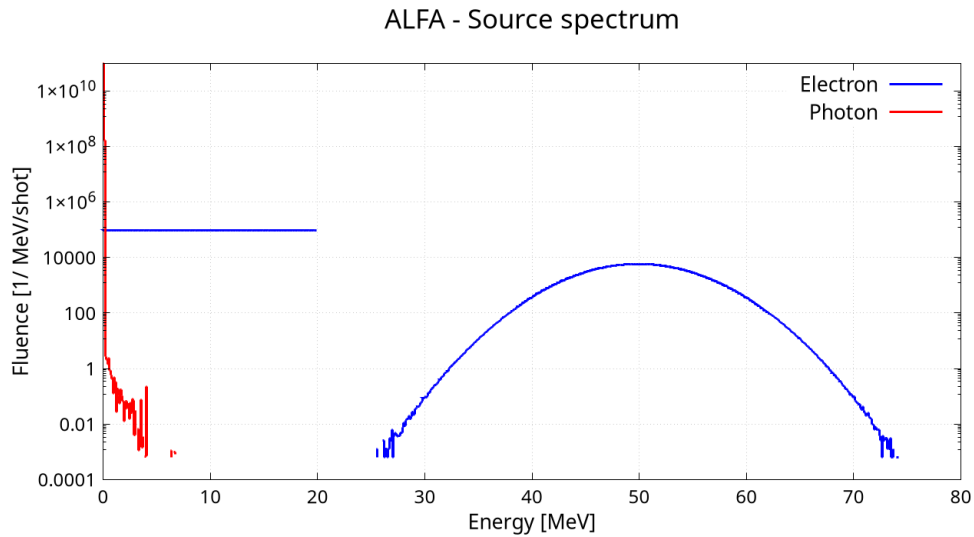


Figure 5.10: FLUKA plot illustrating the source term spectrum resulting from a simulation run with 10^5 primary particles. The red line indicates the photon beam, the uniform blue distribution on the left side corresponds to the low-energy background electron beam, and the Gaussian blue distribution represents the QME electron beam.

6. Measurements and Data Analysis

6.1. Dataset

The dataset refers to the measurement campaign of 11-15 March 2024, encompassing a full week of irradiation experiments at ALFA. **Figure 6.1** provides an initial overview of the dataset, illustrating the distribution of laser bursts throughout the week. The plotted data represent the dose rates recorded by the three detectors during this selected period: Lupin (neutrons only), Nausicaa (gamma particles only), and Pandora (showing only the gamma component for visualization purposes).

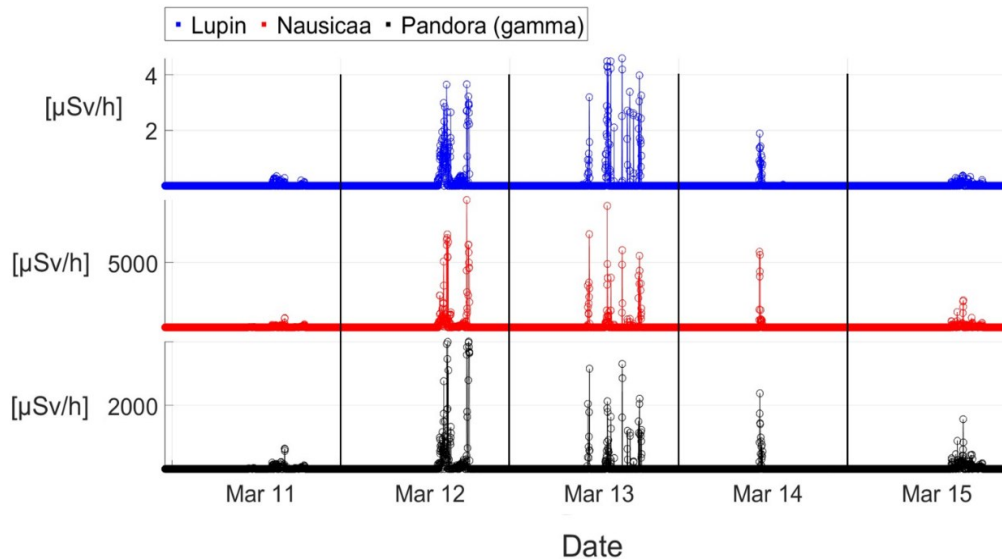


Figure 6.1: Plots of the dose-rates detected in the ALFA experimental hall during 5 days of irradiation. Each subplot refers to the measurements of a single dosimeter. From top to bottom: the Lupin, the Nausicaa, the Pandora (only the gamma particles component).

Each peak of the plot represents a cluster of bursts that cannot be individually distinguished for two reasons. The first reason is technological, relating to the frequency at which the dosimeter electronics record the signal from the detector. Since this frequency is lower than the rate at which the shots are delivered (10 kHz), each peak appears as a convolution of multiple shots. The second reason pertains to the plotting configuration, which is too broad to allow for discrimination between closely spaced peaks. To address this latter issue, some of the following plots will focus on data corresponding to a single day of irradiation. However, the results and conclusions will be drawn by examining the whole dataset.

Furthermore, considering that the Pandora dosimeter is equipped with two distinct and independent detection channels (see Paragraph 5.2) the following description will address gammas and neutrons separately. This approach will facilitate a more detailed analysis and a side-by-side comparison between the Lupin-Pandora (for neutrons) and Nausicaa-Pandora (for gamma particles) systems.

6.2. Neutrons

Figure 6.2 illustrates the dose-rates recorded by the Lupin dosimeter and the neutron component of the Pandora dosimeter during operations on March 13, 2024.

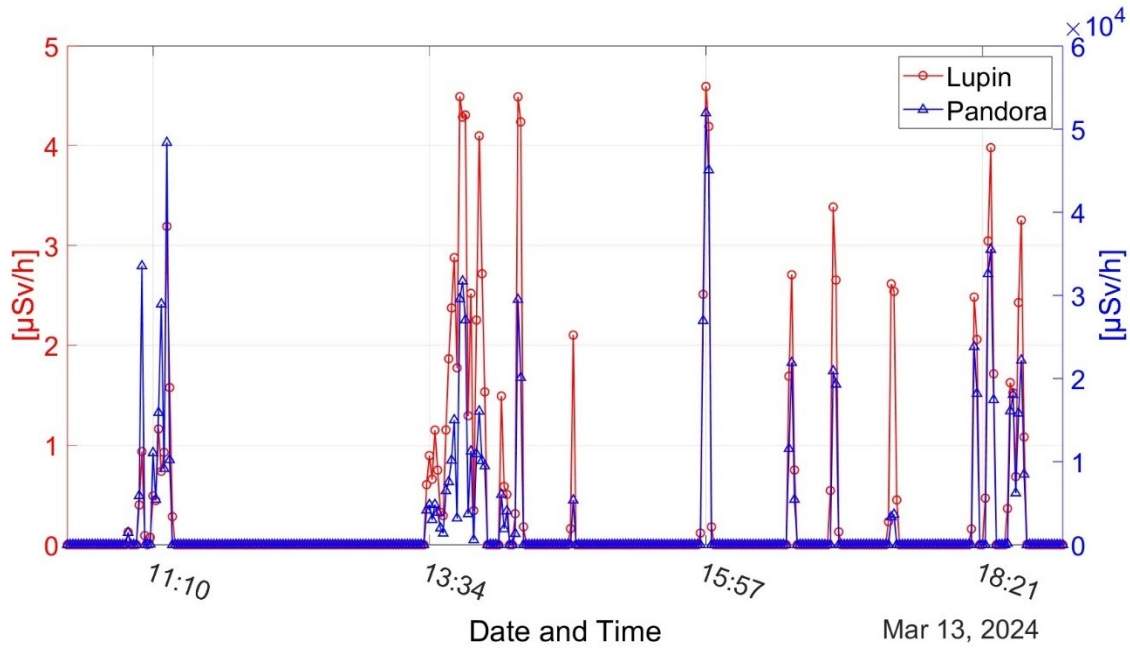


Figure 6.2: Plot of the dose-rates detected in the ALFA experimental hall by the Lupin dosimeter (represented by red circles) and the Pandora dosimeter (represented by blue triangles). Due to the differing orders of magnitude of the dose-rates recorded by the two dosimeters, the Lupin data is plotted against the left vertical axis, while the Pandora data is plotted against the right vertical axis.

The dose rates recorded by the two dosimeters are represented on distinctly different scales, necessitating the use of separate vertical axes for the two plots. Specifically, the peaks detected by the Lupin dosimeter reach $4.5 \mu\text{Sv/h}$, whereas those recorded by the Pandora exceed $5 \cdot 10^4 \mu\text{Sv/h}$, demonstrating a remarkable difference of four orders of magnitude. This pattern is consistently observed throughout the entire week.

A valuable feature of the Pandora readout electronics is the ability to separate high-energy neutrons from low-energy neutrons, with a threshold set at 20 MeV. This capability enables a comparison of the two components, facilitating a better understanding of potential misdetections. **Figure 6.3** presents a plot of the dose rates for low-energy and high-energy neutrons.

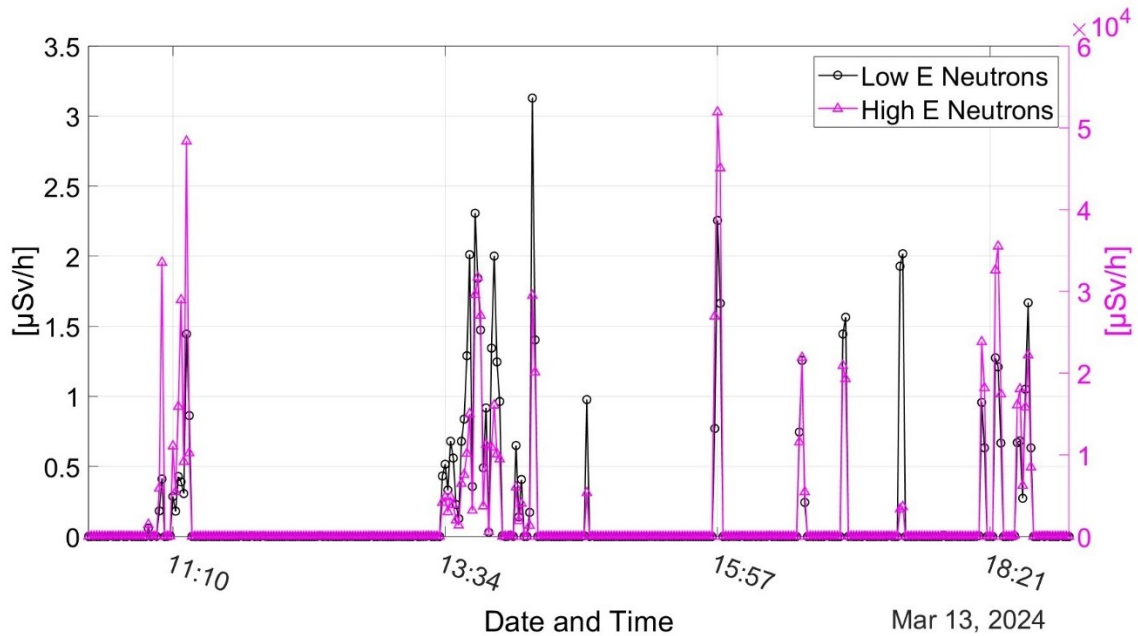


Figure 6.3: Plot of the neutrons dose-rates detected in the ALFA experimental hall by the Pandora dosimeter. The low-energy component is represented by the black curve plotted against the left vertical axis, while the high-energy component is depicted by the pink curve plotted against the right vertical axis.

As illustrated, the significant dose-rate is primarily attributed to the high-energy neutron component detected by the Pandora dosimeter. While the peaks in the dose-rate for the low-energy neutron (represented in black) component are comparable to those detected by the Lupin dosimeter, the peaks associated with the high-energy component (represented in pink) are on the order of 10^4 $\mu\text{Sv/h}$.

Given that it is not possible to determine a priori which dosimeter may be misdetecting the true dose, further considerations are warranted. For instance, an examination of the source spectrum plotted in **Figure 5.9** indicates that a low number of neutrons are expected to be produced with energies exceeding 20 MeV. Since secondary particles can be generated with energies equal to or lower than those of the primary particles that produced them, only high-energy electrons can indirectly contribute to this production. Specifically, electrons

can generate neutrons through electronuclear reactions; however, the cross section for this type of reaction is quite small. The most probable mechanism for neutron production in this context involves gamma rays generated by bremsstrahlung, inelastic scattering, and pair production. These gamma rays can subsequently produce neutrons via photonuclear reactions.

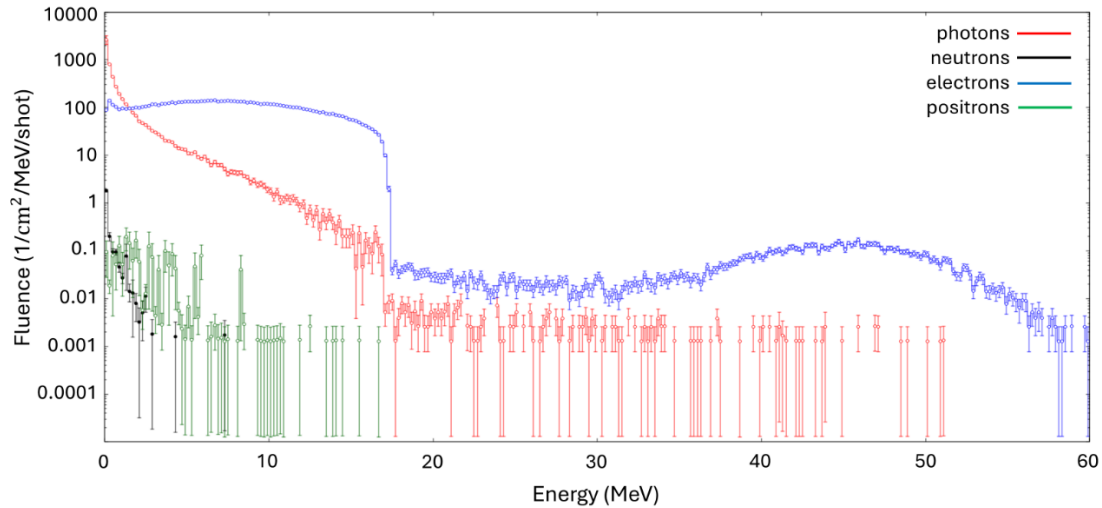


Figure 6.4: FLUKA plot illustrating the fluence across the mockup detector positioned close to the beam dump.

The assertion that the number of neutrons with energies above 20 MeV is low is supported by the fluence obtained from the Monte Carlo simulation conducted with the parameters detailed in Paragraph 5.4. The fluence is measured across a plane positioned at the same location as the actual detector and is normalized to 1 MeV per shot. As shown in **Figure 6.4**, the results of the Monte Carlo simulation indicate that the majority of neutrons do not exceed 5 MeV. Although there are significant systematic uncertainties associated with the simulations (see Paragraph 5.1), it is highly unlikely that a substantial number of neutrons have been produced at higher energies. The energies of the produced neutrons are primarily determined by the cross sections of the photonuclear production channels, and minor modifications to

the setup are unlikely to have a drastic impact on the results. Consequently, it is suggested that the dose-rates recorded in the high-energy neutron channel of the Pandora dosimeter may not be reliable in this context.

The following analysis focuses temporarily on the low-energy component of the Pandora, in comparison with the dose rate recorded by the Lupin. Since each dosimeter captures data from the electronics at slightly different frequencies, or the convolution of the ultra-short pulses may vary, a viable solution is to calculate the integral of each individual peak and compare it with the corresponding integral of the peaks recorded by the other detector. This integration is performed using an algorithm that automatically identifies the data samples associated with the same peak by detecting the minimum values among two consecutive peaks. Subsequently, the integral is calculated between two adjacent minima. This integration method helps to mitigate synchronization issues between the datasets. **Figure 6.5** presents a histogram that compares the integrated dose of the peaks recorded by the two dosimeters throughout the entire week. Overlaying the histogram is a graph that illustrates the ratio of the doses detected by the two dosimeters.

The average ratio between the integrated doses of the two dosimeters is 3.4, meaning that the dose detected by the Lupin is, on average, three times higher than the dose detected by the Pandora. This discrepancy, as discussed above, cannot be attributed to the fact that only the low-energy neutron component of the Pandora dosimeter has been considered, since the amount of neutrons with energies exceeding 20 MeV should be negligible. On the other hand, this discrepancy is in accordance with the literature, which shows a higher underestimation of the dose at high dose-rates by the Pandora with respect to the Lupin BF3 [35].

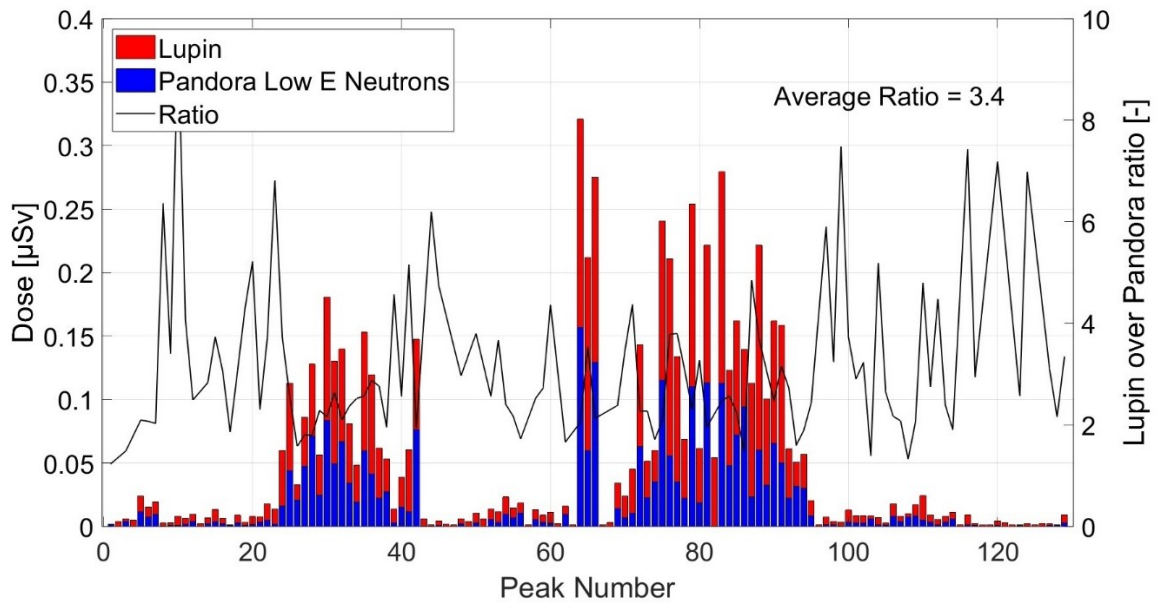


Figure 6.5: Histogram of the integral of each peak evaluated from the neutrons dose rate detected by the Lupin dosimeter (represented in red), compared with the corresponding peak integral for the low-energy neutron component detected by the Pandora dosimeter (represented in blue). The black curve illustrates the computed ratio between the integrated doses of the two dosimeters.

The doses delivered by neutrons during the period from March 11 to March 15, 2024, are summarized in **Table 6.1**. This table provides an overview of the radiation levels to which the dosimeters were exposed, as well as a broader understanding of the secondary radiation field surrounding the ALFA experimental station. The results indicate that the dosimeter recorded irradiation events for approximately 5 hours throughout the week, with a total delivered dose ranging from 3.12 to 6.36 μSv for the Pandora and Lupin dosimeters, respectively. On average, the dose rate recorded during the irradiation period was between 0.60 and 1.21 $\mu\text{Sv/h}$, with peak dose rates observed on March 13, 2024, reaching values between 3.13 and 4.59 $\mu\text{Sv/h}$.

Date	Irradiation Time	No. of Peaks	Dose [μSv]		Average Dose-Rate [$\mu\text{Sv/h}$]		Max Dose-Rate [$\mu\text{Sv/h}$]	
			P	L	P	L	P	L
March 11, 2024	47m 26s	19	0.087	0.147	0.110	0.186	0.181	0.346
March 12, 2024	2h 9m 46s	47	1.35	2.73	0.510	1.02	1.98	3.66
March 13, 2024	1h 13m 21s	23	1.34	2.91	1.09	2.39	3.13	4.59
March 14, 2024	20m 10s	5	0.165	0.348	0.487	1.03	0.804	1.89
March 15, 2024	1h 9m 50s	33	0.129	0.218	0.111	0.186	0.243	0.368
Total	5h 10m 33s	127	3.12	6.36	0.601	1.22	3.13	4.59

Table 6.1: Summary of the irradiation campaign conducted from March 11 to March 15, 2024. ‘Irradiation Time’ and ‘Number of Peaks’ are determined using an algorithm that identifies instances when the dose rate exceeds a specified threshold (i.e., background). ‘Average Dose Rate’ represents the mean of the dose rate values recorded during those time intervals. The columns “P” and “L” differentiate the results obtained by Pandora and Lupin, respectively.

6.3. Gamma Particles

The discussion regarding the dose delivered by gamma particles is more straightforward, as no anomalies similar to those observed in the neutron measurements have been detected. However, some discrepancies between the Nausicaa dosimeter and the Pandora dosimeter are still present. **Figure 6.6** displays a comparison of the doses recorded by both dosimeters on March 13, 2024. As observed, the doses recorded by the Nausicaa dosimeter are generally about double those recorded by the Pandora dosimeter. This trend is consistent across the other days in the dataset.

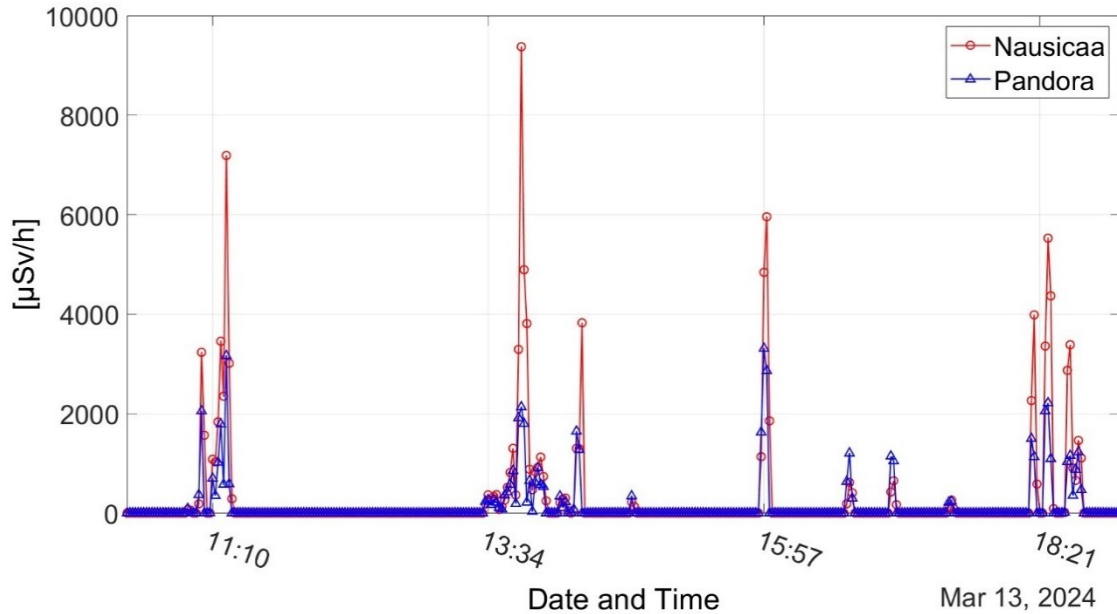


Figure 6.6: Plot of the gamma particle dose-rates (in $\mu\text{Sv/h}$) measured in the ALFA experimental hall on March 13, 2024.

To further investigate the differences in the performance of the two dosimeters, a peak-to-peak integration analysis can be conducted, similar to that performed for the neutron dose component. **Figure 6.7** presents a histogram comparing the integrated peak values obtained for the Nausicaa dosimeter with those corresponding to the Pandora dosimeter, along with the peak-to-

peak ratio between the two results. The findings indicate that the average ratio is 1.5, with Nausicaa consistently detecting higher doses in the majority of cases.

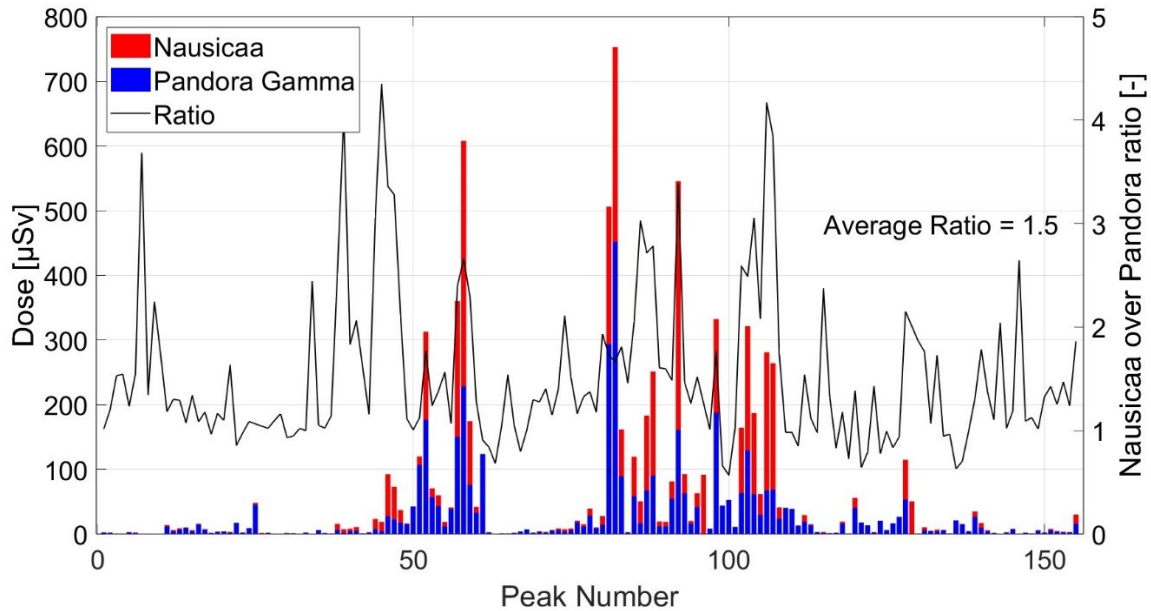


Figure 6.7: Histogram of the integral of each peak evaluated from the gamma particles dose-rate detected by the Nausicaa dosimeter (represented in red), compared with the corresponding peak integral detected by the Pandora dosimeter (represented in blue). The black curve illustrates the computed ratio between the integrated doses of the two dosimeters.

Despite the observed discrepancy between the dose measurements obtained from the Nausicaa and Pandora detectors, such a result is anticipated given the challenging environmental conditions. As anticipated, none of the detectors utilized in this study are specifically designed to accurately measure dose rates as high as those encountered in the vicinity of the ALFA station. Consequently, a factor of 1.5 difference between the measurements from the two dosimeters is considered an acceptable outcome.

Date	Irradiation Time	No. of Peaks	Dose [μSv]		Average Dose-Rate [$\mu\text{Sv/h}$]		Max Dose-Rate [$\mu\text{Sv/h}$]	
			P	N	P	N	P	N
March 11, 2024	3h 4m 26s	40	208.4	219.5	67.4	71.2	639.5	714.6
March 12, 2024	2h 50m 25s	43	2400	3828	835.1	1350	4015	9833
March 13, 2024	1h 13m 23s	22	1285	2686	1068	2207	3311	9377
March 14, 2024	20m 8s	6	331.6	675.2	975.7	2006	2383	5833
March 15, 2024	2h 55m 46s	44	492.7	569.4	168.1	195.1	1569	2088
Total	10h 13m 8s	155	4718	7990	462.1	780.6	4015	9833

Table 6.2: Summary of the irradiation campaign conducted from March 11 to March 15, 2024. ‘Irradiation Time’ and ‘Number of Peaks’ are determined using an algorithm that identifies instances when the dose rate exceeds a specified threshold (i.e., background). ‘Average Dose Rate’ represents the mean of the dose rate values recorded during those time intervals. The columns “P” and “N” differentiate the results obtained by Pandora and Nausicaa, respectively.

Table 6.2 provides a general overview of the radiation levels associated with the gamma particle component surrounding the ALFA station, summarizing the doses delivered by gamma particles during the period from March 11 to March 15, 2024. The data reveal that the dosimeter detected irradiation events for approximately 10 hours over the course of the week, with total delivered doses ranging from 4718 to 7990 μSv for the Pandora and the Nausicaa dosimeters, respectively. The average dose rate during the irradiation period was found to be between 462.1 and 780.6 $\mu\text{Sv/h}$. Notably, peak dose rates were recorded on March 12, 2024, with values ranging from 4015 to 9833 $\mu\text{Sv/h}$.

6.4. High Energy Neutrons

The high-energy neutron doses detected by the Pandora dosimeter appear to be unreliable in this context for the reasons outlined above. However, it would be valuable to investigate the mechanisms underlying this behavior and to identify the specific dose-rates at which it can be observed. One potential explanation is that the ultra-short, high-intensity bursts of gamma radiation impacting the detector are being misidentified as high-energy neutrons. In support of this hypothesis, **Figure 6.8** illustrates a clear correlation between the dose rates of high-energy neutrons and gamma particles.

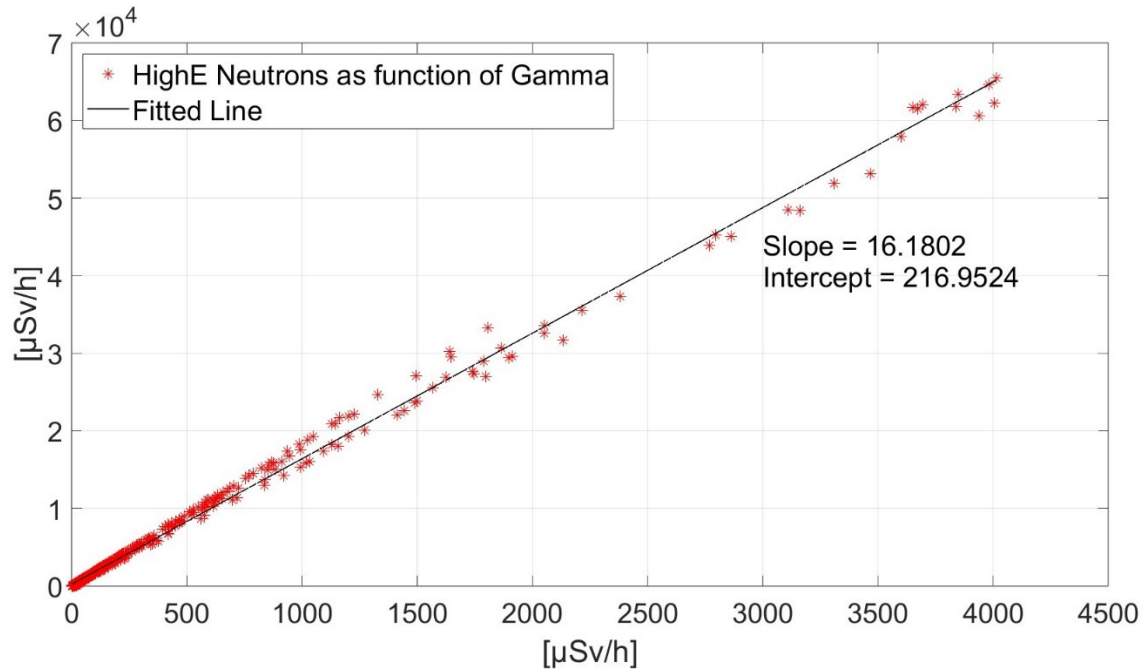


Figure 6.8: Plot of the dose-rate of the high-energy neutron component detected by the Pandora dosimeter as a function of the gamma particle dose-rate. The black line represents the linear regression of the occurrences referring to values higher than 1 $\mu\text{Sv/h}$.

To further investigate the results of this analysis, an R-squared test was conducted. The R-squared value is a statistical measure that represents the proportion of variance in the dependent variable (in this case, the high-energy neutron dose-rate) that can be explained by the independent variable (in this case, the gamma particles dose-rate) in a regression model. The formula for calculating R-squared is as follows:

$$R^2 = 1 - \frac{SS_{res}}{SS_{tot}}$$

Where:

- $SS_{res} = \sum_{i=1}^n (y_i - \hat{y}_i)^2$ is the residual sum of squares, with n representing the number of observations, y_i as the observed value

of the dependent variable, and \hat{y}_i as the predicted value from the regression model;

- $SS_{tot} = \sum_{i=1}^n (y_i - \bar{y})^2$ is the total sum of squares, where y_i again denotes the observed value of the dependent variable and \bar{y} is the mean of the observed values.

R-squared values range from 0 to 1. A value of 0 indicates that the model does not explain any of the variability in the dependent variable, while a value of 1 suggests that the model accounts for all the variability.

The R-squared value obtained from this interpolation indicates a very high correlation, measuring 0.997. In contrast, the analysis of the correlation between the high-energy and low-energy neutron components yields an R-squared value of 0.670. While this value is still relatively high, reflecting the simultaneous production of all types of radiation, it is notably lower compared to the correlation observed between high-energy neutrons and gamma particles.

Additional information can be obtained from the examination of the two supplementary Pandora dosimeters located in the vicinity of the experimental hall. One dosimeter is situated in the control room, several meters away from the beam, while the other is positioned in the west corridor, directly on the opposite side of the wall adjacent to the beam dump (see **Figure 5.6**). **Figures 6.9** and **6.10** present the dose-rate plots recorded by the Pandora dosimeter in the west corridor and in the ALFA control room, respectively.

The plots for the Pandora dosimeter positioned in the west corridor indicate that the secondary radiation reaching this area is significantly lower compared to the dose rates observed in the ALFA hall. However, the second plot in **Figure 6.9**, which pertains to the high-energy neutron channel, again exhibits anomalous behavior, with peaks exceeding 100 $\mu\text{Sv/h}$. In contrast, the low-

energy neutron channel maintains peaks below 1 $\mu\text{Sv/h}$. The observation that both dosimeters (i.e., the one located inside the experimental hall and the one in the west corridor) exhibit the same anomalous behavior suggests that the misdetection is not attributable to a defective dosimeter, but rather to its inherent design. While the possibility that both detectors may be faulty cannot be entirely ruled out, it is considered unlikely.

In contrast, the plots for the Pandora dosimeter positioned in the control room (**Figure 6.10**) do not exhibit the same effect. In the high-energy neutron channel, only a stochastic signal attributable to background radiation is recorded, while the other two channels continue to display radiation peaks. Dose rate levels in the control room are expected to be considerably low due to the distance from the source and the high angle relative to the beam direction. Consequently, it is presumed that the very low dose rates detected in the gamma particle and low-energy neutron channels are accurately measured. Additionally, the background signal recorded in the high-energy neutron channel is considered reliable for the same reasons. Therefore, the Pandora dosimeter in this instance does not exhibit any anomalous behavior, suggesting that the misdetection of high-energy neutrons is a threshold phenomenon that occurs when the dosimeter is exposed to high dose-rate values.

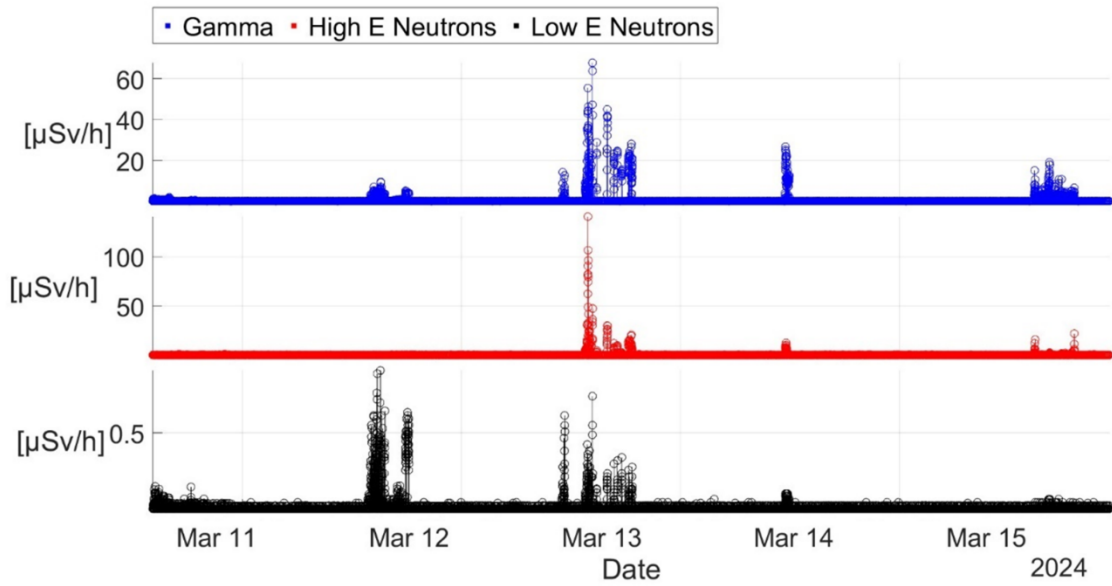


Figure 6.9: Plots of the dose-rates detected in the west corridor, close to the ALFA experimental hall, during 5 days of irradiation by a Pandora dosimeter. Each subplot refers to a single radiation component. From top to bottom: gamma particles, high-energy neutrons, low-energy neutrons.

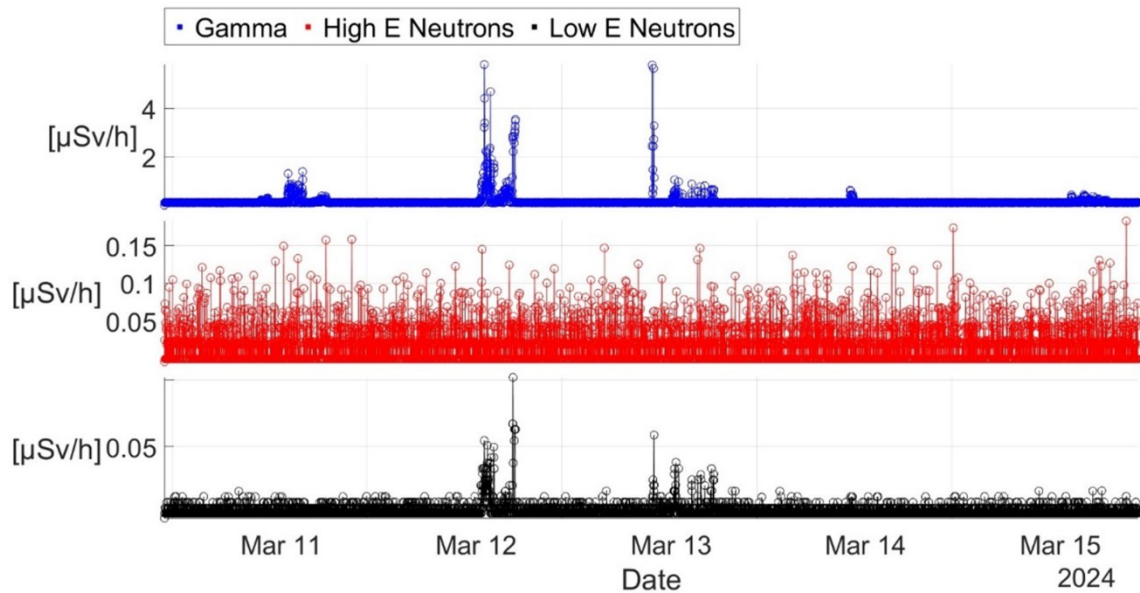


Figure 6.10: Plots of the dose-rates detected in the control room of the ALFA experimental hall, during 5 days of irradiation by a Pandora dosimeter. Each subplot refers to a single radiation component. From top to bottom: gamma particles, high-energy neutrons, low-energy neutrons.

Finally, a detailed examination of the irradiation campaign conducted between 17:00 and 19:30 on March 13, 2024, is presented. Comprehensive information regarding the irradiation process during this time period has been made available by the experimental group and the specifics of the irradiations are summarized in **Table 6.3**.

#	Time	Duration	Irradiation Setup	Beam Charge
1	17:00	120 s	Double GAFs separated by two slabs of 2 cm each	$11 \cdot 10^4 e^-$
2	17:40	50 ms opening of the gas nozzle at 10 Hz for 100 s	Reassembled ICRU phantom, 164 mm from glass, 9 cm of slab in total, 10 GAFs every cm.	$5 \cdot 10^4 e^-$
3	18:05	Same as #2	Same as #2	Same as #2
4	18:30	Same as #2	Same as #2 and a big magnet with 15 mm opening to deflect away low-energy beams from ICRU phantom	Same as #2
5 & 6	19:15	60 s test + 120 s session	Liquid dosimeters and two GAFs.	$9 \cdot 10^4 e^-$

Table 6.3: Specifics of the irradiations conducted on March 13, 2024, between 17:00 and 19:30. The ICRU phantom is a standardized physical model used in radiation dosimetry to simulate human tissue for the purpose of measuring and calculating radiation doses. GAF stands for Gafchromic film and is a type of radiochromic film used for measuring radiation doses. The number of electrons (e^-) for each beam is an estimate and the time of the irradiation is approximate.

Irradiations #2 to #4 employ the same setup and irradiation duration, which also implies a similar estimated beam charge delivery. However, irradiation #4 incorporates a magnet specifically designed to divert the low-energy component of the radiation. Due to the neutrality of the neutron particle, it is expected that the three peaks corresponding to irradiations #2 to #4 will exhibit similar values in both the high-energy and low-energy neutron channels. It is also expected that the gamma particle peak associated with irradiation #4 will be lower than those of irradiations #2 and #3. This reduction is attributed to the decrease in bremsstrahlung radiation directed toward the dosimeters, resulting from the diversion of the charged particle component of the beam (i.e., electrons).

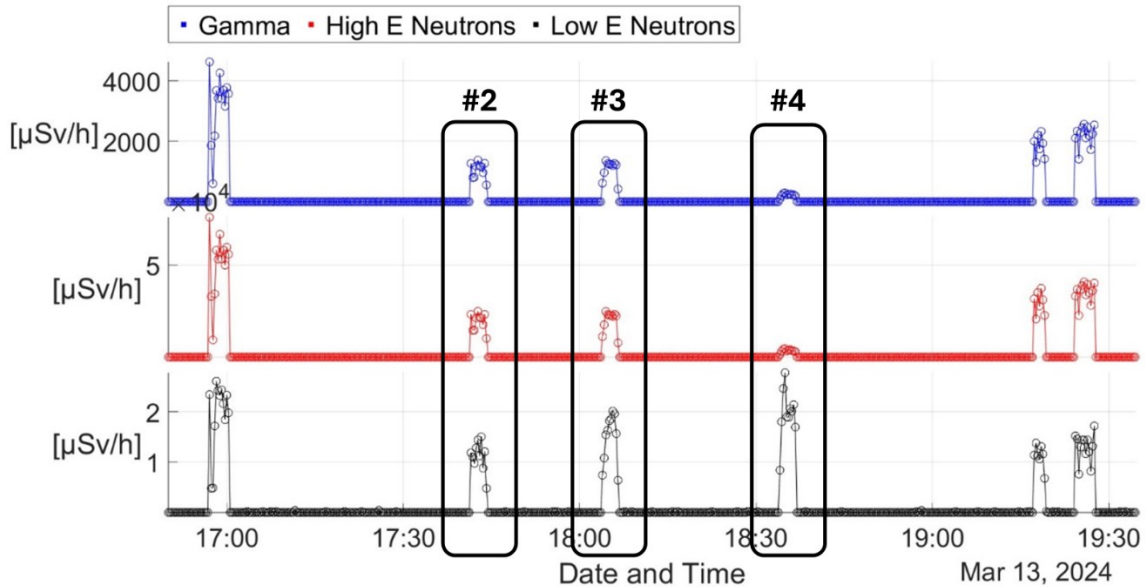


Figure 6.11: Plots of the dose-rates detected by a Pandora in the ALFA experimental hall on March 13, 2024, between 17:00 and 19:30. Each subplot refers to a single radiation component. From top to bottom: gamma particles, high-energy neutrons, low-energy neutrons.

Figure 6.11 presents the dose-rate plots recorded by the Pandora dosimeter positioned near the beam dump during the examined time period. Notably, the high-energy neutron and gamma particle channels exhibit identical radiation profiles, characterized by two peaks of approximately equal magnitude, with the latter peak being significantly smaller. In contrast, the low-energy neutron channel displays three similar peaks, consistent with the neutral nature of neutrons, which cannot be deflected by a magnetic field.

This finding further supports the hypothesis that the high-energy neutron channel of the Pandora dosimeter is influenced by gamma particle radiation. In this instance, the correlation is suggested by physical considerations rather than by numerical data analysis, as discussed previously. This reinforces the body of evidence and simultaneously reduces the likelihood of erroneous data manipulation.

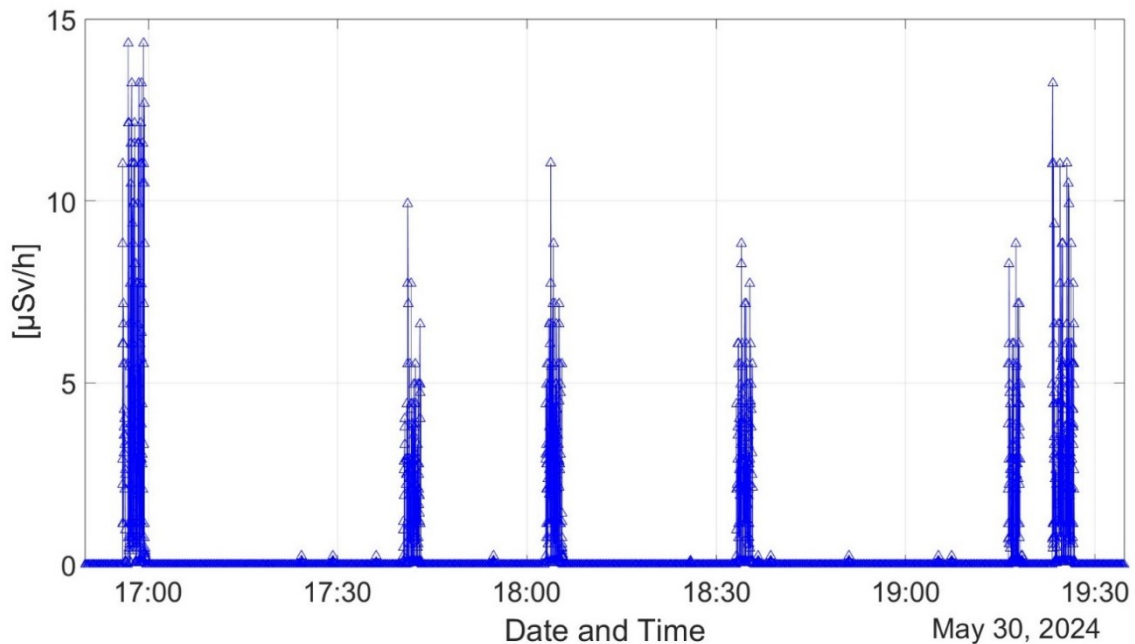


Figure 6.12: Plot of the dose-rates detected by a Lupin dosimeter in the ALFA experimental hall on March 13, 2024, between 17:00 and 19:30. Each group of peaks corresponds to one of the irradiations described in Table 6.1.

For reference, **Figure 6.12** displays the dose rates recorded by the Lupin dosimeter under the same conditions. The plot of the radiation levels detected by the Lupin indicates that peaks #2, #3, and #4 are similar to one another, as expected.

7. Conclusions

The objective of the present study was to investigate the secondary radiation field in the vicinity of the ALFA experimental station, while simultaneously evaluating the response of three commercially available dosimeters in this environment. This research was motivated by the rapid advancement of laser-driven accelerators and their potential applications, which necessitate precise dosimetry of the secondary radiation field for both radiation safety and operational purposes.

This study began with an overview of laser-driven acceleration technology, focusing specifically on the ELI project and the ELI Beamlines facility, with particular emphasis on the ALFA experimental station. Subsequently, the work presented fundamental concepts in dosimetry, along with a discussion of the challenges associated with dosimetry in a laser-driven acceleration environment. Additionally, a concise overview of the Monte Carlo method was provided, highlighting its utility and limitations for dosimetry in this context. Finally, a detailed description of the dosimeters and the experimental setup employed during the data collection campaign was included.

The analysis of the data collection campaign was conducted separately for neutrons and gamma particles to facilitate a one-to-one comparison of dosimeters and to enhance the understanding of each radiation component. The results for neutrons revealed a discrepancy between the measurements recorded by the Lupin dosimeter and the Pandora dosimeter, exhibiting a remarkable difference of four orders of magnitude.

However, a closer examination of the data from the Pandora indicated that this discrepancy was due to the high-energy neutron channel of the detector. In contrast, the results from the Lupin dosimeter, when compared to the low-energy neutron channel of the Pandora, remained within a factor of 3.4. This level of difference is considerably more acceptable and understandable in the unique environment surrounding a laser-driven accelerator. Consequently, the neutron dose rate averaged over 5 hours of irradiation was found to be between 0.6 and 1.2 $\mu\text{Sv/h}$ for the Pandora (considering only the low-energy neutron channel) and the Lupin, respectively, with total dose deliveries of 3.1 and 6.4 μSv .

In terms of the gamma particle component, the comparison indicated general agreement between the Pandora and Nausicaa dosimeters, with the latter recording doses that were 1.5 times higher than those of the Pandora. This difference is again acceptable and somewhat expected in a working environment for which the dosimeters were not specifically designed. The average dose rates recorded by the two devices during the week of irradiation were 482 $\mu\text{Sv/h}$ for the Pandora and 781 $\mu\text{Sv/h}$ for the Nausicaa, while the total doses detected over 11 hours of irradiation were 4.7 mSv and 8.0 mSv, respectively.

Conversely, the high-energy neutron channel of the Pandora dosimeter was supposed to be not completely reliable due to the negligible amount of neutrons anticipated based on the source term described in Paragraph 5.4. This assessment was further supported by a Monte Carlo simulation of the irradiation at ALFA carried out with the FLUKA4-4.0 code. Consequently, the study concentrated on investigating this potential malfunction of the Pandora dosimeter.

Initially, a strong correlation between the high-energy neutron and gamma particle channels was identified through statistical analysis. Following this, an examination of data collected from two additional Pandora dosimeters positioned in the vicinity of the experimental hall was conducted. This analysis revealed that the dosimeter located in the west corridor, adjacent to the beam dump, still exhibited a correlation between the high-energy neutron and gamma particle channels, despite the dose levels being significantly lower (two orders of magnitude lower) than those recorded inside the experimental hall, where the other Pandora dosimeter was situated. In contrast, the Pandora dosimeter placed in the control room, where dose rates were even lower, did not display the anomaly in the high-energy neutron channel, instead recording only the expected background signal. These findings suggest that the anomalous behavior of the Pandora dosimeter is not attributable to a faulty device; rather, it appears to be associated with high dose rate levels.

Finally, an examination of specific irradiation setups and the corresponding measurement data from the Pandora detector indicated that the high-energy neutron channel is, in some way, related to the doses recorded in the gamma particle channel based on physical considerations. This last finding is particularly valuable in ruling out the possibility that the observed correlation could be due to inaccuracies in statistical data handling.

Further and more detailed studies will be necessary to identify the cause of the anomalous behavior exhibited by the Pandora dosimeter. For example, controlled radiation environments could provide additional insights into the conditions that give rise to this phenomenon. Additionally, a thorough examination of the front-end electronics will be required to determine whether the issue originates from signal processing or from the detector itself.

In general, this study represents an initial and modest step toward understanding the secondary radiation field in the vicinity of a laser-driven accelerator, and further advanced studies will be necessary to enhance this research. The use of passive detectors may be beneficial in mitigating pile-up and dead time effects during the data collection process. Additionally, the development of new dosimeters specifically designed to withstand very high dose rates, strong electromagnetic pulses (EMPs), and potentially capable of detecting various radiation components will be essential for future investigations.

References

- [1] Danson C.N. *et al.*, High Power Laser Science and Engineering, **7**, e54 (2019).
- [2] Esarey E. *et al.*, Reviews of Modern Physics, **81(3)**, 1229-1285 (2009).
- [3] Albert F. and Thomas A.G.R., Plasma Phys. Control. Fusion, **58**, 103001 (2016).
- [4] Schippers J.M. *et al.*, Seminars in Radiation Oncology, **28(2)**, 150-159 (2018).
- [5] Tisi M., *Secondary neutrons at laser-driven ion sources*, Ludwig Maximilian University of Munich (2023).
- [6] Svelto O., *Principles of Lasers*. Springer, New York, 2010.
- [7] McClung F.J. and Hellwarth R.W., J. Appl. Phys. **33**, 828–829 (1962).
- [8] Di Domenico M., J. Appl. Phys. **35**, 2870–2876 (1964).
- [9] Baumgartner R. and Byer R., IEEE Journal of Quantum Electronics **15**, 6 (1979).
- [10] Strickland D. and Mourou G., Opt. Commun. **56** 219–21 (1985).
- [11] Hooker S.M., Nature Photonics **7**, 772-785 (2013).
- [12] Budker G.I., Proc. CERN Symposium on High Energy Accelerators **1**, 68 (1956).
- [13] Tajima T. and Dawson J.M., Phys. Rev. Lett. **43(4)**, 267 (1979).
- [14] Albert F., *et al.*, New J. Phys. **23** 031101 (2021).
- [15] Guénot D. *et al.*, Nat. Photon. **11**, 293–6 (2017).
- [16] Kim T.H. *et al.*, Appl. Sci. **2021**, 11, 583.

- [17] https://research-and-innovation.ec.europa.eu/strategy/strategy-2020-2024/our-digital-future/european-research-infrastructures/eric_en
- [18] Korn G. *et al.*, ELI –Extreme Light Infrastructure Whitebook, Science and Technology with Ultra-Intense Lasers, THOSS Media GmbH, Berlin, Germany, (2011).
- [19] The Extreme Light Infrastructure ERIC Annual Report 2022-2023, ELI ERIC (2023).
- [20] <https://www.llnl.gov/>
- [21] <https://www.nationalenergetics.com/>
- [22] <https://ekspla.com/>
- [23] Cimmino A. *et al.*, Nuclear Science and Engineering **198**, 245-263 (2024).
- [24] Zymak I. *et al.*, 22nd European Conference on Radiation and Its Effects on Components and Systems (RADECS), Venice, Italy, 1-4 (2022).
- [25] Lazzarini C.M. *et al.*, Phys. Plasmas **31**, 030703 (2024).
- [26] Laitano R.F., *Fondamenti di dosimetria delle radiazioni ionizzanti*, ENEA, 2011.
- [27] Operational quantities and new approach by ICRU. Annals of the ICRP. 2016; 45(1_suppl):178-187.
- [28] *Quantities and Units in Radiation Protection Dosimetry*, The International Commission on Radiation Units and Measurements, ICRU Report 51, ICRU, Bethesda (1993).
- [29] Jansen A.A., Journal of Nuclear Medicine Technology **8**, 241-241 (1980).

- [30] 1990 Recommendations of the International Commission on Radiological Protection. ICRP Publication 60. Ann. ICRP **21** (1-3), 1991.
- [31] Consoli F. *et al.*, High Power Laser Sci. Eng., **8**, e22, 59 (2020).
- [32] Horváth D. *et al.*, Phys. Med. Biol. **68** 22NT01 (2023).
- [33] Knoll G. F., *Radiation Detection and Measurement*. vol. 69 (2010).
- [34] Caresana M. *et al.*, Nuclear Instruments and Methods in Physics Research A **737**, 203–213 (2014).
- [35] Caresana M. *et al.*, Rev. Sci. Instrum. **85**, 065102 (2014).
- [36] Swanson W.P., Health Physics Vol **35** (1978).
- [37] Swanson W.P., Health Physics Vol. **37** (1979).
- [38] Weber S. *et al.*, Matter Radiat. Extremes **2**, 149 (2019).
- [39] Zio E., *The Monte Carlo Simulation Method for System Reliability and Risk Analysis*, Springer-Verlag, London (2013).
- [40] Metropolis N. and Ulam S., Journal of the American Stat. Ass., 44:247, 335-341 (1949).
- [41] Andreo P., Radiation Oncology, 13:121, (2018).
- [42] Sarrut D. *et al.*, Medical Physics **41**, 064301 (2014).
- [43] Böhlen T.T. *et al.*, Nuclear Data Sheets **120**, 211-214 (2014).
- [44] Ferrari A. *et al.*, *FLUKA: a Multi-Particle Transport Code*, CERN-2005-010, Geneve (2005).
- [45] Vlachoudis V., *Flair: A powerful but user friendly graphical interface for Fluka*, 04 2009.
- [46] Mao X.S. *et al.*, Nucl. Instr. And Methods **562-2**, 963-966 (2006).
- [47] Li X. *et al.*, Nucl. Instr. And Methods, **1039** (2022).
- [48] Lari L. *et al.*, *FLUKA-MARS15 simulations to optimize the Fermilab PIP-II movable beam absorber*. United States (2019).
- [49] Chiti M. *et al.*, Radiation Measurements, **176** (2024).

- [50] Boccone V. *et al.*, Nuclear Data Sheets **120**, 215-218 (2014).
- [51] Böhlen T. T. *et al.*, Nuclear Data Sheets **120**, 211-214 (2014).
- [52] Cimmino A. *et al.*, Nuclear Science and Engineering **198**, 245-263 (2024).
- [53] Olšovcová V. *et al.*, Progress in Nuclear Science and Technology **4**, 173-177 (2014).
- [54] Strabel C. *et al.*, EPJ Web of Conferences **153**, 07026 (2017).
- [55] Enghbrecht F. S. *et al.*, J. Radiol. Prot., **40** 1048 (2020).
- [56] Scuderi V. *et al.*, Appl. Sci. **8**, 1415 (2018).
- [57] Klett A. *et al.*, Radiation Measurements **45**, 1242-1244 (2010).
- [58] Aza E. *et al.*, Radiation Measurements **61**, 25-32 (2014).
- [59] <http://www.elsenuclear.com/en/>
- [60] http://www.elsenuclear.com/media/k2/attachments/DAT_LUPIN_EN_1.11.pdf
- [61] http://www.elsenuclear.com/media/k2/attachments/DAT_IONCHAMBERDET_EN_1.12.pdf
- [62] Vascotto A. *et al.*, RADSYNCH'09, 65-70 (2009).
- [63] <https://www.berthold.com/en/>
- [64] <https://www.desy.de/>
- [65] <https://www.struck.de/>
- [66] Leake J. W. *et al.*, Nucl. Instr. and Methods in Physics Research A **613**, 112–118 (2010).
- [67] <https://www.lesker.com/viewports/viewports-iso-flanged-kodial-glass/part/vpzl-160>
- [68] <https://www.eli-beams.eu/facility/bezpecnost-prace-ochrana-zdravi-a-zivotniho-prostredi/>

List of Figures

2.1	Schematic representation of a laser and its main components.	5
2.2	Focused intensity progress in time.	7
2.3	Schematic representation of the acceleration of electrons in a LWFA. In this case, the plasma is produced by ionization of the gas released by a gas inlet in correspondence of the focusing point of the laser.	9
2.4	ELI Beamlines laser building schematic view.	13
2.5	Scheme of ALFA experimental station.	17
3.1	Relationship between the protection quantities and operational quantities for use in dosimetry.	18
3.2	ICRU sphere in an aligned and expanded field. The point at which the ambient dose equivalent $H^*(d)$ is determined is located at depth d within the sphere along the radius of the sphere opposite to the alignment direction of the field.	24
3.3	Examples of phantoms (a, b, c) made of tissue-equivalent material with different shapes for the calibration of dosimeters in terms of personal dose equivalent $H_p(d)$.	26
3.4	Time required to deposit 99% of the total dose. The scoring bin size is 2 mm (radial) \times 3 mm (longitudinal). Time scoring is done with 400 fs time bins.	28
3.5	Fraction of photonuclear reactions produced in the electromagnetic cascades initiated by an incident electron on thick targets per unit of beam power, as a function of the energy of the electron.	31
4.1	Inverse transform method for continuous distributions. It is clear from the figure that $P(X < x) = P(R < r)$, relation that can be retrieved from $P(X \leq x) = P(R \leq F_X(x))$ and $F_X(x) = r$.	37

4.2	Screenshot of the Input section of the FLAIR interface for FLUKA.	40
5.1	Photograph and scheme of the LUPIN area monitor (dimensions in centimeters).	45
5.2	Instrument linearity.	49
5.3	Image of a portion of the ALFA experimental hall. The ALFA vacuum chamber is highlighted within the red rectangle.	50
5.4	CAD drawing of the ALFA vacuum chamber and its components. Top (a) and side (b) view.	51
5.5	Top view of the FLUKA geometry model of the ALFA experimental hall.	52
5.6	Setup of dosimeters for the measurement campaign in the ALFA experimental hall.	52
5.7	FLUKA geometry model of a portion of the ALFA experimental station, side view.	52
5.8	FLUKA geometry model of the ALFA vacuum chamber and its components, side view. Each square of the grid has a side length of 10 cm.	54
5.9	FLUKA plot illustrating the source term spectrum resulting from a simulation run with 10^5 primary particles.	55
6.1	Plots of the dose-rates detected in the ALFA experimental hall during 5 days of irradiation. Each subplot refers to the measurements of a single dosimeter.	56
6.2	Plot of the dose-rates detected in the ALFA experimental hall by the Lupin dosimeter (represented by red circles) and the Pandora dosimeter (represented by blue triangles).	58
6.3	Plot of the neutrons dose-rates detected in the ALFA experimental hall by the Pandora dosimeter.	59
6.4	FLUKA plot illustrating the fluence across the mockup detector positioned close to the beam dump.	60
6.5	Histogram of the integral of each peak evaluated from the neutrons dose rate detected by the Lupin dosimeter (represented in red), compared with the corresponding peak integral for the low-energy neutron component detected by the Pandora dosimeter (represented in blue).	62

6.6	Plot of the gamma particle dose-rates (in $\mu\text{Sv/h}$) measured in the ALFA experimental hall on March 13, 2024.	64
6.7	Histogram of the integral of each peak evaluated from the gamma particles dose-rate detected by the Nausicaa dosimeter (represented in red), compared with the corresponding peak integral detected by the Pandora dosimeter (represented in blue).	65
6.8	Plot of the dose-rate of the high-energy neutron component detected by the Pandora dosimeter as a function of the gamma particle dose-rate.	68
6.9	Plots of the dose-rates detected in the west corridor, close to the ALFA experimental hall, during 5 days of irradiation by a Pandora dosimeter. Each subplot refers to a single radiation component.	71
6.10	Plots of the dose-rates detected in the control room of the ALFA experimental hall, during 5 days of irradiation by a Pandora dosimeter. Each subplot refers to a single radiation component.	71
6.11	Plots of the dose-rates detected by a Pandora in the ALFA experimental hall on March 13, 2024, between 17:00 and 19:30. Each subplot refers to a single radiation component.	73
6.12	Plot of the dose-rates detected by a Lupin dosimeter in the ALFA experimental hall on March 13, 2024, between 17:00 and 19:30.	74

List of Tables

2.1	Present and Target Parameters of the Laser Systems at ELI Beamlines.	15
2.2	Main experimental stations of ELI Beamlines.	16
5.1	Main features of the utilized dosimeters.	44
5.2	Nuclear reactions with carbon as target material used in the LB 6419.	48
5.3	Characteristics of the source term components.	55
6.1	Summary of the irradiation campaign conducted from March 11 to March 15, 2024.	63
6.2	Summary of the irradiation campaign conducted from March 11 to March 15, 2024.	66
6.3	Specifics of the irradiations conducted on March 13, 2024, between 17:00 and 19:30.	72

